

Cepheid-based Distances to NGC 4303 and NGC 1068

MADISON MARKHAM ¹, MISTY C. BENTZ ¹, LAURA FERRARESE ², CHRISTOPHER A. ONKEN ³ AND
MARIANNE VESTERGAARD ^{4,5}

¹*Department of Physics and Astronomy, Georgia State University, Atlanta, GA 30303, USA*

²*NRC-Herzberg Astronomy and Astrophysics, 5071 West Saanich Road, Victoria, BC, V9E 2E7, Canada*

³*Research School of Astronomy and Astrophysics, Australian National University, Canberra, ACT 2611, Australia*

⁴*DARK, Niels Bohr Institute, University of Copenhagen, Jagtvej 155, DK-2200 Copenhagen*

⁵*Steward Observatory and Department of Astronomy, University of Arizona, 933 N Cherry Avenue, Tucson AZ 85721, USA*

ABSTRACT

We present Cepheid-based distances to two canonical AGN: NGC 4303 (M 61) and NGC 1068. Data were obtained using the *Hubble Space Telescope* with nonredundant time spacing over 12 visits for each target, and observations were made with the F555W and F814W filters. We found 32,694 point sources in NGC 4303, and 130 of these were determined to be strong Cepheid candidates with periods ranging $\sim 13 - 93$ days. In NGC 1068, we found 20,207 point sources, where 51 of these were strong Cepheid candidates with periods $\sim 14 - 92$ days. We fit the period–luminosity relationship, calibrated based on a geometric distance to the LMC by Riess et al. (2019), to our Cepheid candidates in each galaxy and correct for potential effects of metallicity. Using a distance constraint for the LMC given by Pietrzyński et al. (2019), this yields a distance modulus of $\mu = 31.083 \pm 0.035$ mag for NGC 4303 and $\mu = 30.150 \pm 0.106$ mag for NGC 1068. Thus, we measure distances of $D = 16.47 \pm 0.27$ Mpc to NGC 4303 and $D = 10.72 \pm 0.52$ Mpc to NGC 1068.

Keywords: Cepheid distance (217) — Seyfert galaxies (1447) — AGN host galaxies (2017)

1. INTRODUCTION

Henrietta Leavitt’s work with Cepheid variable stars (Leavitt & Pickering 1912) remains some of the most influential in extragalactic astronomy to date. Her discovery of the period–luminosity relationship (also known as the Leavitt Law) allowed for the distance to the Andromeda galaxy to be measured for the first time (Hubble 1925), unlocking the distance scale of the Universe. Over a century later, modern extragalactic studies have been revolutionized by the success of the *Hubble Space Telescope* (*HST*). The *HST* Key Project was one significant endeavor with the goal of determining the Hubble constant using Cepheids (Freedman et al. 2001). Recently, Cepheids have been observed using *HST* in numerous successful studies to obtain accurate distances to nearby active galactic nuclei (AGN; e.g., Bentz et al. 2019; Yuan et al. 2020, 2021), Type Ia Supernova (SN Ia) host galaxies (e.g., Saha et al. 2006; Riess et al. 2022), and the Magellanic Clouds (e.g., Riess et al. 2019; Breuval et al. 2024).

In addition to its importance in Cepheid studies, one of the more surprising discoveries by *HST* was that all massive galaxies likely host supermassive black holes

(SMBHs) at their centers. This has inspired a wealth of research on SMBHs and galactic evolution, and SMBHs have been found to coevolve with their hosts (e.g., Kormendy & Ho 2013). Correlations of SMBH mass with bulge velocity dispersion ($M_{\text{BH}} - \sigma_*$; Ferrarese & Merritt 2000; Gebhardt et al. 2000; Gültekin et al. 2009) and bulge luminosity ($M_{\text{BH}} - L_{\text{bulge}}$; Kormendy & Richstone 1995; Kormendy & Ho 2013) are interpreted to mean that active black holes affect their host galaxies on massive scales, far greater than their gravitational influence. AGN feeding and feedback processes seem to play an essential role in galactic evolution, and SMBHs lie at the centers of these systems.

Accurate distances to nearby AGN are some of the most crucial measurements to be made of these objects, and large uncertainties in distance measurements inhibit useful measurements of several other important characteristics, such as central black hole mass. Many direct black hole mass measurements (which have been made for both targets in our sample) rely on spatial resolution, and this is directly related to distance. Unlike AGN at cosmological distances, nearby AGN are not all reliably within the Hubble Flow; thus, redshift-independent dis-

tances are required. NGC 4151, for example, is one of the most widely studied Seyfert 1 AGN; it is an incredibly valuable observational resource for feeding and feedback studies as one of the nearest and brightest AGN (e.g., Ulrich 2000). Its distance was previously quoted as a group average, with four members ranging 3.9 – 34 Mpc (Tully et al. 2009). Recent work by Yuan et al. (2020) was able to constrain the distance to NGC 4151 to 15.8 ± 0.4 Mpc using Cepheids observed with *HST*.

Seyfert 2 AGN are distinct from Seyfert 1 AGN by a viewing angle-imposed obscuration of the SMBH with a dusty torus. NGC 1068, in particular, was instrumental in creating a unified AGN model through the discovery of broad Balmer lines in the polarized light from this Seyfert 2 galaxy (Antonucci & Miller 1985). High angular-resolution studies of the obscuring molecular gas result in a better understanding of the structure of the torus (e.g. in NGC 1068, GRAVITY Collaboration et al. 2020; Gámez Rosas et al. 2022, 2025), and determining physical size from angular size depends directly on distance. Understanding the structure of the torus then allows for better-fitting models for the spectral energy distributions (SEDs) of AGN. Furthermore, describing AGN luminosity with these models requires accurate distances, which NGC 1068 lacks. Another canonical Seyfert 2, NGC 4303, is a popular target for spatial studies on star formation in spiral galaxies — in particular, it is included in the Physics at High Angular resolution in Nearby GalaxieS (PHANGS) program (Schinnerer et al. 2019). Emsellem et al. (2022) describe the need for understanding characteristics such as star formation timescales and stellar feedback processes at spatially-resolved scales in nearby galaxies, and the PHANGS-MUSE survey is working to address this. However, the assumed distance for NGC 4303 directly affects the spatial scale of star formation in this galaxy, among other things. We therefore set out to rectify the lack of accurate distances to these two canonical AGN by using *HST* observations to detect and characterize Cepheids in their host galaxies.

NGC 4303 (also known as M61) is a late-type Sbc galaxy with a double bar and a nuclear starburst region (Binggeli et al. 1985; Schinnerer et al. 2002; see Figure 1). It is classified as a Seyfert 2 AGN, and Pastorini et al. (2007) derive a central black hole mass of $M_{\text{BH}} = 5.0_{-2.3}^{+0.9} \times 10^6 M_{\odot}$ using STIS observations of ionized gas kinematics. These authors assume a distance of 16.1 Mpc (Schinnerer et al. 2002, using the results of Ferrarese et al. 1996), which corresponds to a scale of $1'' \approx 78$ pc. Redshift-independent distance measurements have primarily been obtained using Tully–Fisher and Type II supernovae (SNe II) methods, and these

measurements span a range of $\sim 7 - 20$ Mpc (Bottinelli et al. 1984; Rodríguez et al. 2014). NGC 4303 is nearly face-on ($i = 25^\circ$ from ^{12}CO velocity fields; Schinnerer et al. 2002), which contributes to large uncertainties in distances derived using the Tully–Fisher method. Additionally, though it has hosted an incredible number of supernovae (8 known since 1926!), none of them have been Type Ia and suitable as standard candles. However, two of those supernovae were Type IIP supernovae (SNe IIP), and there have been recent attempts to use SNe IIP as standardizable candles (Csörnyei et al. 2023). Anand et al. (2021) attempted to constrain its distance using the tip of the red giant branch (TRGB) method, however their results were inconclusive. NGC 4303 has been studied in the context of the starburst–AGN connection (e.g., Riffel et al. 2016; Dametto et al. 2019), though the results are limited by the large uncertainties in distance. Furthermore, the association of NGC 4303 with the Virgo cluster is uncertain (Binggeli et al. 1985), and therefore the influence of the Virgo cluster on the star formation rate in NGC 4303 is also uncertain. An accurate distance is necessary to better understand feeding and feedback processes between the AGN and nuclear starburst region.

NGC 1068 is one of the best-studied Seyfert galaxies; it belongs to the original sample of 12 Seyfert galaxies (Seyfert 1943), and it is often described as the prototypical Seyfert 2 AGN. NGC 1068 is an Sb galaxy with a weak bar visible in the NIR and a circumnuclear starburst ring (Telesco et al. 1984; Scoville et al. 1988; Thronson et al. 1989; Davies et al. 1998; see Figure 1). Lodato & Bertin (2003) constrained its black hole mass to $M_{\text{BH}} = 8.0 \pm 0.3 \times 10^6 M_{\odot}$ using water maser kinematics, assuming a distance of 14.4 Mpc and a scale of $1'' \approx 69$ pc. The disk is moderately inclined, having an inclination angle of $i = 40 \pm 3^\circ$ from observations of H I gas kinematics (Brinks et al. 1997). Famously, NGC 1068 is also an archetype of AGN unification schemes (e.g., Antonucci & Miller 1985; Konigl & Kartje 1994). NGC 1068 is therefore a fantastic laboratory for studies of feeding and feedback processes, specifically through emission-line observations in the central disk. AGN-driven outflows of dense molecular gas have been revealed (e.g., García-Burillo et al. 2014), and this has inspired studies on the structure and kinematics of molecular gas in the torus of NGC 1068, such as recent work by Gámez Rosas et al. (2025). Despite this, its distance has been neglected. Similar to NGC 4303, its distance has primarily been constrained using the Tully–Fisher method, with many studies adopting 14.4 Mpc from Tully & Fisher (1988). Recently, Tikhonov & Galazutdinova (2021) determined a TRGB distance of

11.14 ± 0.54 Mpc, though this was accomplished using inhomogeneous archival *HST* data. A more accurate distance to NGC 1068 is thus needed for crucial measurements of AGN feedback processes.

This paper is organized as follows. Section 2 provides descriptions of the observations for each target. Section 2.1 outlines the photometric techniques employed to determine light curves for all point sources, while Section 3 explains our criteria for selecting Cepheid candidates among these sources. In Section 4, we fit the resulting period–luminosity relationships, and we considered the potential effects of metallicity. We discuss previous distance measurements to each target in Section 5, as well as the implications of our Cepheid-based distances. Finally, Section 6 provides a summary.

2. OBSERVATIONS

Multi-epoch observations for each target were obtained with the *HST* Wide Field Camera 3 (WFC3)⁶. We observed in two optical bandpasses (F555W & F814W) with the UVIS channel, which has a field of view of $2.6' \times 2.6'$ and a pixel scale of $0.04''$. We selected the UVIS-FIX aperture to ensure a fixed field center and aid in data analysis. Similarly, we planned the visits with a fixed roll angle. Observations in each filter employed a four-point dither pattern to increase the sampling of the point spread function (PSF) and fill in the physical gap between the two UVIS detectors.

Cepheids are known to have greater pulsation amplitudes at bluer wavelengths; however, bluer wavelengths are more susceptible to extinction (Freedman et al. 1994). Thus, the F555W filter maintained a good compromise for maximizing variability while minimizing reddening effects. We also gathered observations in the F814W filter, which is less sensitive to variability and minimally affected by reddening. This provided us with color information for selecting Cepheid candidates.

Observations of NGC 4303 were taken between April and June of 2023, spanning a total of 70.93 days. NGC 1068 was observed between December 2023 and February 2024 over a period of 70.61 days. Further details of our observing cadence can be found in Table 1.

We scheduled 12 total visits with nonredundant time spacing. For each target, images were taken in the F555W filter, and five of these visits included F814W observations adopting the same position and orientation. In the case of NGC 4303, two of the visits did not achieve guide star lock, and one of these two visits was

Table 1. Observations

Visit	UT	Filter	Exposure Time (s)
NGC 4303			
1	2023 Apr 19	F814W	2356
2	2023 Apr 30	F555W	2364
3	2023 May 6	F555W	2364
	...	F814W	2356
4	2023 May 11	F555W	2364
5	2023 May 14	F555W	2364
6	2023 May 17	F555W	2364
7	2023 May 19	F555W	2364
	...	F814W	2356
8	2023 May 21	F555W	2364
9	2023 Jun 3	F555W	2364
	...	F814W	2356
10	2023 Jun 10	F555W	2364
11	2023 Jun 20	F555W	2364
	...	F814W	2356
12	2023 Jun 29	F555W	2364
NGC 1068			
1	2023 Dec 19	F555W	2364
	...	F814W	2356
2	2024 Jan 5	F814W	2356
3	2024 Jan 10	F555W	2364
4	2024 Jan 14	F555W	2364
5	2024 Jan 19	F555W	2364
	...	F814W	2356
6	2024 Jan 21	F555W	2364
7	2024 Feb 2	F555W	2364
	...	F814W	2356
8	2024 Feb 10	F555W	2364
9	2024 Feb 17	F555W	2364
	...	F814W	2356
10	2024 Feb 23	F555W	2364
11	2024 Feb 25	F555W	2364
12	2024 Feb 28	F555W	2364

re-observed at the end of the monitoring sequence. The visit that was re-observed required us to adopt a different roll angle, and we chose to minimize the difference between the new roll angle and our previous roll angle to ensure the maximum possible overlap of the FOV for the final visit compared to the previous visits. Observations of NGC 1068 were plagued by similar issues. Four visits did not achieve guide star lock for the F555W observations, and three of these were rescheduled for the end of

⁶ The specific observations analyzed can be accessed from MAST at the Space Telescope Science Institute via [doi: 10.17909/ht8k-kg64](https://doi.org/10.17909/ht8k-kg64).



Figure 1. Red (F814W), blue (F555W), and pseudogreen color images of NGC 4303 (left) and NGC 1068 (right) using *HST* Wide Field Camera 3 data. The field of view of NGC 4303 here is $2.6' \times 2.6'$. This image of NGC 1068 has been cropped to remove a foreground star, and its field of view is $2.1' \times 2.6'$. NGC 4303 is oriented with North approximately up, and NGC 1068 has North oriented 29.22° clockwise from up. Credit: Judy Schmidt.

the monitoring sequence. These visits also required us to adopt different roll angles, and these angles were also kept as close to the original roll angle as possible.

To prepare our observations for analysis of the photometry, we downloaded charge transfer efficiency-corrected images from the Mikulski Archive for Space Telescopes (MAST). The images for each target were registered and drizzled to a common frame using the AstroDrizzle package (Fruchter et al. 2010). First, all observations in F555W were stacked to create a single “deep frame” image for each galaxy. This “deep frame” was then used as a reference for drizzling each of the individual visits in both filters separately. This ensured that all of our images were aligned to a common coordinate frame, so point sources could easily be matched between individual visits.

2.1. Photometry

In general, we followed the same photometric procedure that is outlined in Bentz et al. (2019). For each target, we identified point sources in the field and performed point-spread function (PSF) photometry using DAOPHOT (Stetson 1987).

Beginning with NGC 4303, we used the drizzled F555W deep frame to identify all point sources. We then identified a sample of 89 relatively bright and spatially distinct sources to create a PSF model. These sources were carefully examined for consistency in the shapes of their individual PSFs, so broad profiles, ex-

tended sources, and sources with close neighbors were excluded. The resulting PSF model was used to perform PSF photometry on all point sources in the F555W deep frame. Next, the same sample of 89 stars was used to create PSF models for all of the individual visits in the F555W filter. We selected a new sample of 82 sources to create a PSF model in the F814W filter and all corresponding individual visits. For NGC 1068, we repeated this procedure. We used a sample of 64 stars to construct our PSF model in F555W, and we used a sample of 61 stars in F814W. Aperture corrections for the PSF photometry were derived by calculating the differences between the fitted PSF magnitude and a standard WFC3 10-pixel aperture magnitude for all sources used to create the PSF model. The median difference was accepted as the aperture correction, which yielded brighter corrected magnitudes. Thus, we had unique aperture corrections in F555W and F814W for each target, which were typically found to be around -0.2 mag and -0.3 mag, respectively.

For each galaxy, point sources were matched between visits in F555W and F814W. This yielded 32,694 unique point sources in our field for NGC 4303. Matching point sources similarly in NGC 1068 yielded 20,207 unique point sources. One potential explanation for the increased number of sources in NGC 4303 is the greater star formation rate compared to NGC 1068. Finally, we adopted the magnitude zeropoints for a WFC3 10-pixel aperture given by Riess et al. (2019): 25.727 mag for

F555W and 24.581 mag for F814W in the Vegamag system. In NGC 4303, the typical 10σ depth given the median uncertainty for an individual visit was ~ 26.3 mag in F555W and ~ 25.2 mag in F814W. In NGC 1068, these typical 10σ depths were ~ 26.5 mag in F555W and ~ 25.3 mag in F814W.

3. CEPHEID CANDIDATE SELECTION

To begin our search for variable candidates, we calculated the [Welch & Stetson \(1993\)](#) variability index for each point source, given by:

$$I_V = \sqrt{\frac{1}{n(n-1)} \sum_{i=1}^n \delta V_i \delta I_i} \quad (1)$$

where δV_i and δI_i are the magnitude deviations in F555W and F814W, respectively, relative to the weighted mean magnitudes. The strength of this method comes from the fact that photometric errors should be uncorrelated between images in separate bandpasses. Our criteria for variable objects was a variability index of $I_V > 1.0$, displayed in Figure 2. We chose this criteria to be generous (compared to [Shappee & Stanek \(2011\)](#), for example), as later cuts to other parameters would remove additional unlikely candidates. Based on this selection, we were left with 4,540 variable candidates in NGC 4303 and 1,885 variable candidates in NGC 1068.

Once the variable sources had been identified, we fit the long-period Cepheid templates by [Yoachim et al. \(2009\)](#) to the respective light curves. Following the procedure of [Bentz et al. \(2019\)](#), we injected the fitting routine with a series of 150 initial periods spaced logarithmically between 10 and 100 days. Sources that are true Cepheid candidates should converge to a best-fit period for closely spaced initial guesses near the true period. Each variable source was fit with LMC long period (>10 days) Cepheid templates. Strict limits were set so that periods <10 days or >100 days were not allowed. This ensured that we were not accidentally fitting short-period Cepheids (since we are selecting for long-period Cepheids) and that our observations spanned at least 70% of the period. The successful light curve fits were ranked by χ^2 value, and we examined the six fits with the lowest χ^2 values for each target. We excluded targets where the six best fits found periods that differed by more than 0.3 days. We also excluded those with χ^2 values of straight line fits that were lower than the χ^2 values for the best LMC long-period Cepheid template fit.

In NGC 4303, there were 579 total sources that passed these cuts, spanning a best-fit period range of $10.00 \leq P \leq 93.27$ days. NGC 1068 had 246 sources pass, with

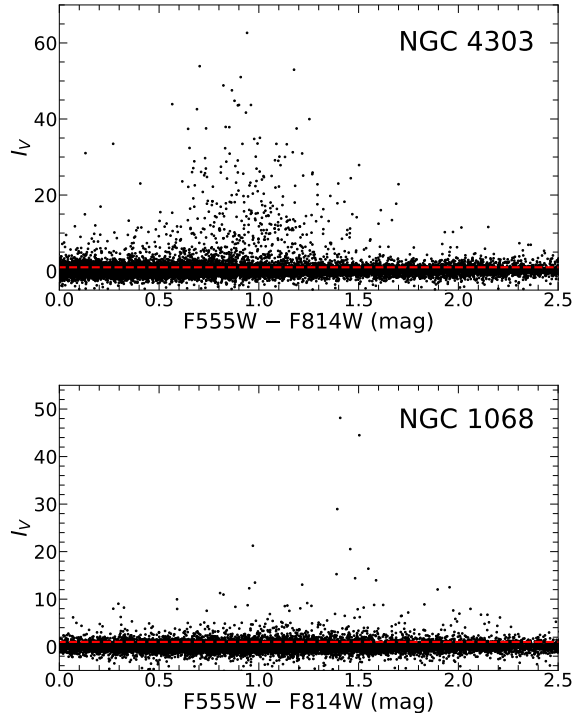


Figure 2. Variability index I_V for point sources in NGC 4303 (top) and NGC 1068 (bottom), shown against color. The red dashed line represents $I_V = 1.0$, so all sources above these lines were considered to be variable candidates.

a best-fit period range of $10.00 \leq P \leq 93.18$ days. For each source, we recorded the period, phase, mean F555W magnitude, and mean F814W magnitude returned by the best-fit light curve parameters.

We then analyzed the colors and amplitudes of these selected targets. Color selections were made based on the expected color of Cepheids on the instability strip ([Shappee & Stanek 2011](#)). We adopted the range $0.5 < F555W - F814W < 2.0$, chosen again to be generous given the small Galactic extinction along our line of sight to these sources ([Bentz et al. 2019](#)). This reduced the number of sources in NGC 4303 from 579 to 435, and in NGC 1068 from 246 to 181. Sources in NGC 1068 were redder on average than sources in NGC 4303, which may be influenced by the greater inclination of NGC 1068. F555W–F814W color uncertainties were restricted to be <0.3 mag ([Bentz et al. 2019](#)), though this only removed a single source from NGC 1068. We also examined the F814W/F555W amplitude ratios based on typical values for fundamental mode pulsators ([Macri et al. 2006](#); [Shappee & Stanek 2011](#)). We found that amplitude ratios of F814W to F555W were all between 0.25 and 0.75 mag, so this criterion also did not remove any sources from either galaxy. We visually ex-

amined the light curves of the selected candidates for strong Cepheid signatures and excluded candidates that do not exhibit the characteristic “sawtooth” variability profile. We were then left with 149 Cepheid candidates in NGC 4303 and 52 Cepheid candidates in NGC 1068.

Finally, we corrected the magnitudes of our remaining Cepheid candidates for the effects of field crowding. Using ADDSTAR, we injected artificial stars randomly into a 40×40 pixel box surrounding each Cepheid candidate. A single star was injected 100 times, yielding 100 different “postage stamp” images for each Cepheid candidate. These artificial stars were randomly assigned magnitudes in the range ± 0.5 mag with respect to the Cepheid candidate magnitude. The same general photometric steps were followed as described above to measure the magnitude of all sources, including the artificial star, in each “postage stamp.” The median difference between the injected magnitudes of the artificial stars and the measured magnitudes of the artificial stars was calculated for each Cepheid candidate, and these differences were then averaged to yield the correction required in each filter to remove the effects of crowding. For NGC 4303, in F555W, the average difference ($m_{\text{injected}} - m_{\text{measured}}$) was 0.011 ± 0.044 mag. In F814W, the average difference was 0.019 ± 0.043 mag. For NGC 1068, the average differences were 0.020 ± 0.046 mag and 0.008 ± 0.033 mag in F555W and F814W, respectively. Since the average differences between the injected magnitudes and measured magnitudes were positive, crowding effects biased the measured magnitudes slightly brighter. To correct for this, the average differences were added to the mean magnitudes for each Cepheid candidate in the two galaxies.

4. PERIOD–LUMINOSITY RELATIONSHIP

For each galaxy, we constructed period–luminosity relationships using the final sample of Cepheid candidates in three different bands—F555W, F814W, and the extinction-free Wesenheit magnitude (W_I , Madore 1982). The Wesenheit magnitudes are given by:

$$W_I = m_{\text{F814W}} - R(m_{\text{F555W}} - m_{\text{F814W}}) \quad (2)$$

where $R = A_I / (A_V - A_I)$. We adopted $R = 1.3$ from Cardelli et al. (1989). Since Wesenheit magnitudes are inherently less susceptible to reddening, there was no need to correct them for Galactic extinction along the line of sight (Madore 1982).

Riess et al. (2019) produced calibrated period–luminosity relationships using Cepheids in the LMC for F555W, F814W, and W_I magnitudes (also using $R = 1.3$). Adopting these calibrations eliminated any additional uncertainties that may be introduced by

converting *HST* filter magnitudes to *V*- and *I*-band magnitudes. The period–luminosity relationship is as follows:

$$m = \alpha \log P + \beta \quad (3)$$

where m is the absolute magnitude in each band, α represents the fixed slope from Riess et al. (2019) calibrations, β represents the intercept in magnitudes, and P is the pulsation period in days.

To fit our sample of Cepheids, we used the SciPy ODR routine (Virtanen et al. 2020). This Levenberg-Marquardt-type algorithm uses an orthogonal distance regression while accounting for uncertainties in both *x*- and *y*-dimensions to return best-fit parameters for the fitting function—in this case, the fitting function was given by Equation 3. Holding the slope fixed to the findings of Riess et al. (2019), we found the intercept in each band. Using the residual variance for each fit returned by the SciPy routine, we calculated σ in each band. Period–luminosity relationships for each band are displayed in Figure 4.

We investigated the possibility of blue blends among our sample, as indicated by sources with observed magnitudes significantly brighter than their corresponding predicted magnitudes. Cepheids that lie in the instability strip span a usual $V - I$ color range of ~ 1 mag (Mochejska et al. 2000). Cepheid candidates observed to be > 1 mag brighter than predicted are likely Cepheids blended with bluer, brighter stars (Shappee & Stanek 2011). Using the same criteria as Bentz et al. (2019), we found no Cepheids in NGC 4303 with $m_{\text{pred}} - m_{\text{obs}} \geq 1.0$ mag in the F555W filter. We found one likely blue blend candidate in NGC 1068, and this reduced our sample from 52 to 51 Cepheid candidates.

Outliers in period–luminosity relationships can most often be attributed to misidentification—either of the mode of oscillations or of the class of variable star (Kodric et al. 2015). To account for these outliers, we followed the recommendation of Kodric et al. (2015) and instituted a 3σ -clipping routine that only applied to the W_I magnitudes. Each time the regression was run, the greatest outlier outside of a 3σ distance was removed and a new fit was determined. This process was done iteratively until there were no more points with $> 3\sigma$ distance from the best fit. The outliers were removed from the other filters, and then the final fits in all three bands were determined and recorded. The final sample for NGC 4303 was reduced from 149 to 130 Cepheid candidates, and for NGC 1068 the sample remained at 51 candidates. The removal of these outliers did not significantly impact the intercept values, though, as the final fits were consistent within the uncertainties with the best-fit intercept before clipping was applied. The

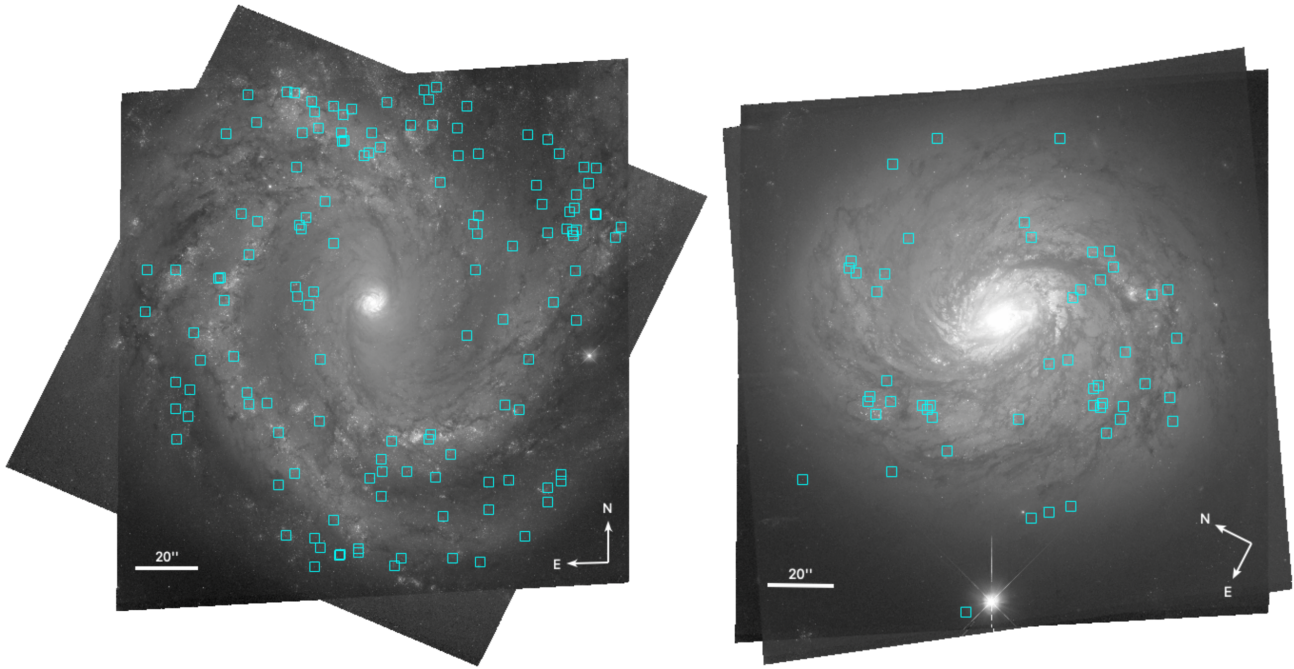


Figure 3. Drizzled “deep frame” F555W-band images of NGC 4303 (left) and NGC 1068 (right) with Cepheid candidate positions marked by cyan boxes. The Cepheid candidates marked here represent our final samples for each galaxy. Compasses are provided in the lower right corners, and 20'' scale bars are provided in the lower left corners.

spatial positions of our final candidates in each galaxy are displayed in Figure 3. Color–magnitude diagrams with 3σ outliers marked are shown in Figure 5. The final best-fit light curve parameters and individual light curves of Cepheid candidates in each galaxy are available in the Appendix, with NGC 4303 Cepheids in Section A and NGC 1068 Cepheids in Section B.

Our sight-lines to both NGC 4303 and NGC 1068 are out of the plane of the Milky Way, and consequently the Galactic extinction is not severe. Schlafly & Finkbeiner (2011) report Galactic extinction in the direction of NGC 4303 to be $A_V = 0.064 \pm 0.040$ mag and $A_I = 0.034 \pm 0.040$ mag; extinction in the direction of NGC 1068 is $A_V = 0.095 \pm 0.040$ mag and $A_I = 0.051 \pm 0.040$ mag. These values were subtracted from the intercepts in their respective filters. Due to the extinction-free nature of Wesenheit magnitudes, no correction was applied to W_I . Taking the LMC intercepts from Riess et al. (2019) with our extinction-corrected best-fit values, we calculated distance moduli to each galaxy relative to the LMC ($\mu_{\text{rel LMC}}$). These values are listed in Table 2.

We tested for incompleteness in our samples by recalculating the W_I intercept over a series of minimum period cuts, shown in Figure 6. There is evidently no dependence on minimum period when determining the distance modulus for NGC 4303, out to a minimum period cut of ~ 50 days. Yuan et al. (2021) found a similar

non-effect when testing for incompleteness in NGC 4051. However, there is a decrease in density around 19.5 days visible in Figure 4, so we chose to remove those candidates with periods < 19.5 days. This left us with 124 Cepheid candidates, which was $\sim 95\%$ of our 3σ -clipped sample. In NGC 1068, there is a hint of incompleteness in our sample at shorter periods. Based on Figure 6, we cut Cepheid candidates with $P < 25$ days from our sample. This left us with 38 Cepheid candidates for our distance determination, or $\sim 75\%$ of our 3σ -clipped sample for NGC 1068.

Pietrzyński et al. (2019) determined a distance modulus to the LMC that is precise to 1% ($\mu_{\text{LMC}} = 18.477 \pm 0.026$ mag); this value is currently the most precise available, and it is derived independently using eclipsing binaries. Using this value, we obtained distance moduli in each band to NGC 4303 (see Table 2). The distance modulus using the 95% sample of W_I magnitudes results in a final distance determination of $D = 16.09 \pm 0.25$ Mpc. The distance moduli we obtained for NGC 1068 are also listed in Table 2. Our 75% sample of W_I magnitudes yields a distance to NGC 1068 of $D = 10.21 \pm 0.49$ Mpc.

4.1. Metallicity Dependence

The effects of metallicity on the period–luminosity relationship have been widely studied and hotly debated. For several decades, work to constrain γ , the correlation factor between the period–luminosity relationship zero-

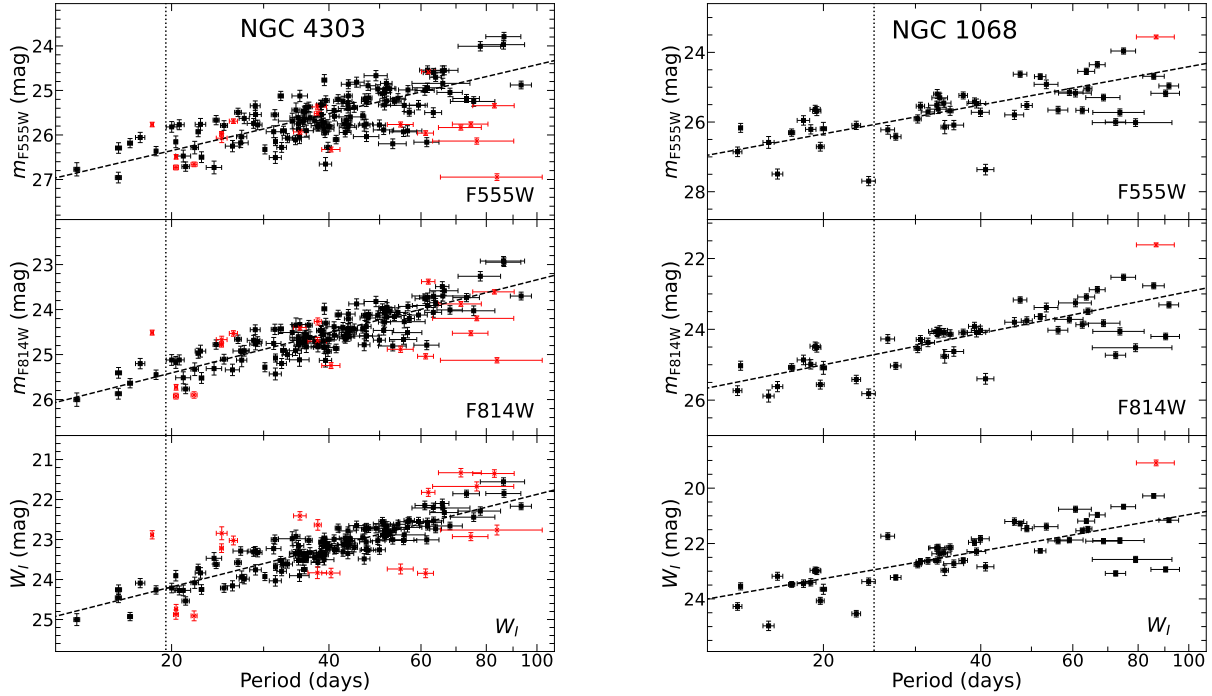


Figure 4. Period–luminosity relationships for Cepheid candidates in NGC 4303 (left) and NGC 1068 (right). The three panels display F555W (top), F814W (middle), and Wesenheit magnitudes (bottom). Red x’s represent Cepheid candidates that were determined to be blue blends or $> 3\sigma$ outliers in the Wesenheit index. The dashed lines in each panel represent the lines of best fit, with fixed slopes based on the findings of Riess et al. (2019). The dotted vertical lines represent points of completeness in our sample—NGC 4303 was visually determined at $P = 19.5$ days, and NGC 1068 was determined from Figure 6 at $P = 25$ days. Corrections for possible metallicity effects and Galactic extinction have not been applied here.

point and metallicity, has yielded inconsistent results. Some authors have proposed that metal-rich Cepheids are systematically fainter (e.g., Romaniello et al. 2008; Bono et al. 2008), though most current debates center around whether the period–luminosity relationship displays a negative ($\gamma < 0 \text{ mag dex}^{-1}$) or null correlation ($\gamma \approx 0 \text{ mag dex}^{-1}$) with metallicity. Of the studies which suggest no significant correlation (e.g., Udalski et al. 2001; Freedman & Madore 2011), Madore & Freedman (2024) currently provide the largest sample in their study, with further support from Madore & Freedman (2025). They compare the zeropoints for 28 nearby ($D \leq 12.5 \text{ Mpc}$) galaxies with distances derived from both Cepheids and the TRGB method, directly updating the work done by Sakai et al. (2004), which found a negative metallicity correlation. Using updated TRGB distances and a slightly larger sample, they find no significant dependence of the reddening-free Wesenheit period–luminosity relationship on metallic-

ity (though see Breuval et al. 2024 for possible limitations of the study).

Other studies suggest that metal-rich Cepheids are brighter than metal-poor ones (e.g., Freedman & Madore 1990; Kennicutt et al. 1998; Sakai et al. 2004; Breuval et al. 2021). Among the authors who suggest a negative correlation of the period–luminosity relationship with metallicity, many find a value of $\gamma \approx -0.25 \text{ mag dex}^{-1}$. Recently, Breuval et al. (2024) re-determined the calibration of the metallicity effect in the *HST* WFC3 photometric system. Using samples of Cepheids with identical-system photometry in the SMC, LMC, and Milky Way galaxies, they find a correlation of $\gamma = -0.264 \pm 0.058 \text{ mag dex}^{-1}$ using W_I magnitudes.

4.1.1. NGC 4303

In addition to the disagreement regarding the effects of metallicity on the Cepheid period–luminosity relationship, there are disagreements in the literature surrounding metallicity gradient values for NGC 4303.

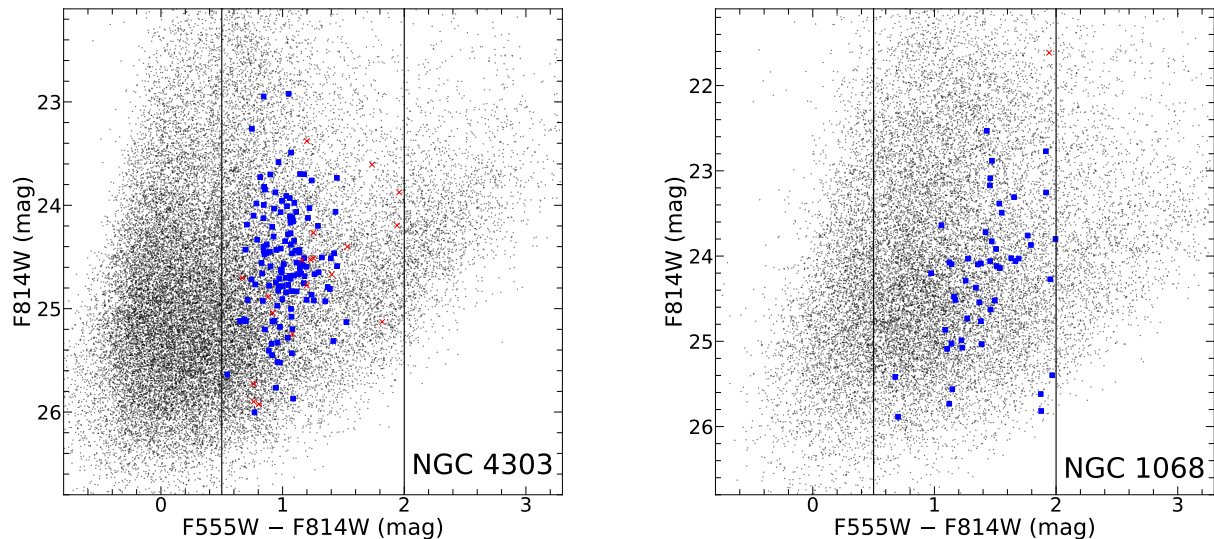


Figure 5. Color–magnitude diagrams of all point sources detected in NGC 4303 (left, shown in black) and NGC 1068 (right, shown in black). The final samples of Cepheid candidates are marked by blue squares, while the blue blends and $> 3\sigma$ outliers are marked by red x’s. Solid vertical lines delimit our range of acceptable $F555W - F814W$ colors.

Martin & Roy (1992) produce an early calculation of $12 + \log([O/H]) = 9.38$ at the galactic center with a radial gradient of -0.076 ± 0.006 dex kpc^{-1} ($-9.8 \pm 0.8 \times 10^{-7}$ dex arcsec^{-1} , from their assumed distance of 15.2 Mpc) based on line ratios from 79 H II regions and using the Edmunds & Pagel (1984) empirical relationship between O/H and $[O \text{ III}]/H\beta$. This relationship was calibrated using $[O \text{ III}] (\lambda 4959 + \lambda 5007)$ and $H\beta$ line measurements in the nuclear regions of NGC 2997 and NGC 7793, plus ten additional H II regions between the two galaxies. The revision of solar composition by Asplund et al. (2005) led to revisions of physical inputs for standard solar models, and this may affect older metallicity determinations. Recent work to update the metallicity gradient has been accomplished by Groves et al. (2023), who produced metallicity gradients for PHANGS galaxies using MUSE observations of nebular regions. They determined a central metallicity of $12 + \log([O/H]) = 8.613$ and a gradient of -0.032 ± 0.006 dex r_{eff}^{-1} for NGC 4303, where r_{eff} is the effective radius containing half of the stellar mass of the galaxy. From their assumption of an r_{eff} of $0.7'$, we converted the gradient from a change in metallicity over physical distance to a change in metallicity over angular distance, which yielded a gradient of $-7.6 \pm 1.4 \times 10^{-4}$ dex arcsec^{-1} . These metallicity calculations employed the empirical relationship by Pilyugin & Grebel (2016) which was calibrated through direct measurements of electron temperature using au-

roral lines of > 300 H II regions across a large sample of galaxies, and Groves et al. (2023) considered it to be the most robust.

To investigate the potential effect of metallicity on our distance determination, we began with the findings of Breuval et al. (2023). The correction to the distance modulus relative to the LMC is given by:

$$\mu_{\text{rel LMC}} = (\beta_{\text{NGC 4303}} - \beta_{\text{LMC}}) + \Delta m \quad (4)$$

where $\beta_{\text{NGC 4303}}$ is our best-fit intercept of the period–luminosity relationship using NGC 4303 Cepheid candidates, and β_{LMC} is the intercept for the LMC period–luminosity fit as reported by Riess et al. (2019). The correction Δm accounts for the difference in metallicity between LMC Cepheids and NGC 4303 Cepheids:

$$\Delta m = -\gamma([O/H]_{\text{NGC 4303}} - [O/H]_{\text{LMC}}) \quad (5)$$

where $[O/H]_{\text{NGC 4303}}$ and $[O/H]_{\text{LMC}}$ are the average metallicities of Cepheids in the two galaxies, and $\gamma = -0.264 \pm 0.058$ mag dex^{-1} (Breuval et al. 2024). We adopted $[O/H]_{\text{LMC}} = -0.32 \pm 0.01$ from Romaniello et al. (2022), relative to a solar abundance of $12 + \log([O/H]) = 8.69$ (Asplund et al. 2009). We used the deprojected angular separations of each Cepheid relative to the center of the galaxy with the gradient by Groves et al. (2023) to determine metallicities at each location. The $[O/H]$ metallicities in our sample of Cepheids candidates ranged from -0.15 to -0.09 dex (relative to solar), with a median of -0.13 ± 0.01 dex.

Table 2. Period–Luminosity Relationships

Band	α	β	σ	$\mu_{\text{rel LMC}}$ (mag)	μ (mag)
NGC 4303					
F555W	−2.76	29.942 ± 0.033	0.525	12.240 ± 0.052	30.717 ± 0.058
F814W	−2.96	29.258 ± 0.023	0.326	12.370 ± 0.046	30.847 ± 0.053
W_I	−3.31	28.491 ± 0.021	0.178	12.556 ± 0.021	31.033 ± 0.033
W_I ($P > 19.5$ days)	−3.31	28.491 ± 0.021	0.181	12.556 ± 0.021	31.033 ± 0.033
Metallicity-corrected W_I ($P > 19.5$ days)	31.083 ± 0.035
NGC 1068					
F555W	−2.76	29.931 ± 0.075	1.058	12.198 ± 0.085	30.675 ± 0.089
F814W	−2.96	28.853 ± 0.066	0.900	11.948 ± 0.077	30.425 ± 0.082
W_I	−3.31	27.575 ± 0.086	0.707	11.640 ± 0.088	30.117 ± 0.091
W_I ($P > 25$ days)	−3.31	27.503 ± 0.100	0.831	11.568 ± 0.100	30.045 ± 0.103
Metallicity-corrected W_I ($P > 25$ days)	30.150 ± 0.106

NOTE—Slopes (α) were held fixed to the values determined from LMC Cepheids by [Riess et al. \(2019\)](#). LMC-relative distance moduli ($\mu_{\text{rel LMC}}$) here have been corrected for extinction but not metallicity as discussed in Section 4. Distance moduli (μ) were determined using an independently measured distance to the LMC by [Pietrzyński et al. \(2019\)](#). Our final adopted distance moduli, after correction for metallicity effects, are provided in bold text.

We calculated the magnitude correction due to metallicity in two ways: first, by adopting a median metallicity for all Cepheid candidates after fitting the period–luminosity relationship and then determining a correction using Equation 5; and second, by using individual Cepheid metallicities with Equation 5 to correct the W_I magnitudes before the fitting and 3σ -clipping procedures. The second method produced an identical 3σ -clipped sample, and both methods yielded the same magnitude correction of $\Delta m = 0.050 \pm 0.012$ mag.

Using Equation 4, we applied this correction of $\Delta m = 0.050 \pm 0.012$ mag to our 95% sample of W_I magnitudes, finding final values of $\mu_{W_I(P > 19.5 \text{ days})} = 31.083 \pm 0.035$ mag and $D = 16.47 \pm 0.27$ Mpc. The inclusion of the Δm correction added 0.38 Mpc to our distance constraint.

4.1.2. NGC 1068

Recent studies have found a slight positive metallicity gradient in NGC 1068 (e.g., [Armah et al. 2024](#); [Amiri et al. 2025](#)). We adopt the metallicity gradient from [Amiri et al. \(2025\)](#), which makes use of MUSE data from the MAGNUM survey ([Mingozzi, M. et al. 2019](#); [Venturi, G. et al. 2021](#)). Using the empirical relationship of [Pettini & Pagel \(2004\)](#), they determined a central metallicity of $12 + \log([\text{O}/\text{H}]) = 8.76$ and a gradient of $2.1 \pm 1.4 \times 10^{-5}$ dex pc^{-1} for NGC 1068. These authors assumed a distance of $D = 12.5$ Mpc, so we converted the gradient to $1.3 \pm 0.8 \times 10^{-4}$ dex arcsec^{-1} . The empirical relationship of [Pettini & Pagel \(2004\)](#) was derived

from nebular [O III] and [N II] lines, and it was calibrated with a sample of 137 extragalactic H II regions. All but six of these H II regions had oxygen abundances determined from electron temperature.

Following the same procedures as for NGC 4303, we first determined the expected metallicity of each Cepheid candidate by using the gradient value and the deprojected angular separations from the galactic center. In NGC 1068, the [O/H] metallicities of our Cepheid candidates spanned 0.073–0.085 dex (relative to solar), with a median of 0.077 dex.

Using Equation 5, we determined both individual corrections and a median correction for our sample of Cepheid candidates. These corrections are in very good agreement, and we adopted the median metallicity correction to the W_I magnitudes of $\Delta m = 0.105 \pm 0.023$ mag.

Finally, we used Equation 4 to correct our W_I distance modulus, where $\Delta m = 0.105 \pm 0.023$ mag. Our metallicity-corrected 75% sample of W_I magnitudes yielded a distance modulus of $\mu_{W_I(P > 25 \text{ days})} = 30.150 \pm 0.106$ mag and a final distance determination of $D = 10.72 \pm 0.52$ Mpc. The inclusion of the Δm correction added 0.51 Mpc to our distance constraint.

5. DISCUSSION

5.1. Previous Distance Measurements

Redshift-independent distance measurements for NGC 4303 span a wide range of values (see Figure 7),

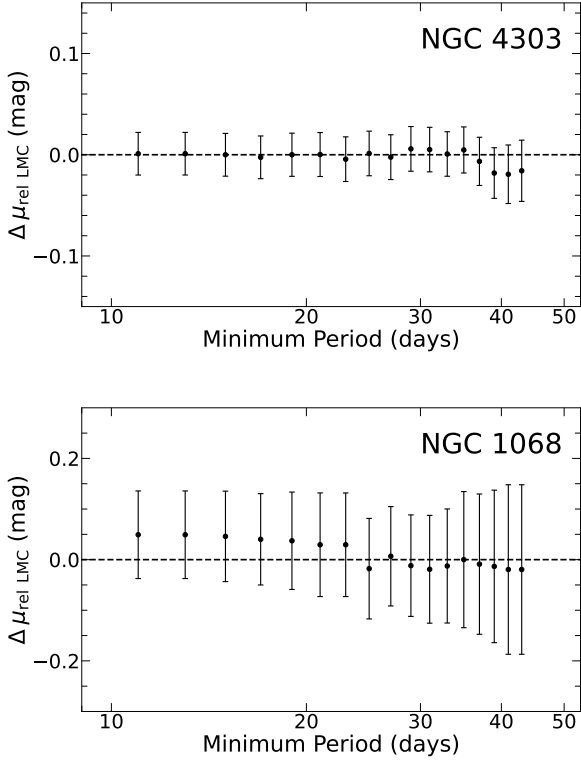


Figure 6. Dependence of $\mu_{\text{rel LMC}}$ on the minimum period of Cepheid candidates in our final sample for NGC 4303 (top) and NGC 1068 (bottom). $\Delta\mu_{\text{rel LMC}}$ is measured relative to the median value over all minimum period cuts. There is no significant evidence for incompleteness in NGC 4303 towards shorter periods, though we do see potential incompleteness in NGC 1068 at $P \lesssim 25$ days.

from 7.59 Mpc using the Tully–Fisher method (Botinelli et al. 1984), to 35.5 Mpc using SNe II (Sparks 1994). One potential complication of Tully–Fisher distance measurements is the inclination angle (Tully & Fisher 1977). NGC 4303 is relatively face-on ($i = 25^\circ$, Schinnerer et al. 2002), which increases the uncertainty in correcting the width of the H I line for the effect of inclination. The most recent distance measurements from this method are 10.1 and 11.0 Mpc by Schöniger & Sofue (1997). Zasov & Bizyaev (1996) provided a similar distance measurement of 10.5 Mpc based on gravitational stability of gas in disks.

Distance measurements made using SNe II methods are mostly based on SN 2008in (Sparks 1994 used SN 1926A, and Csörnyei et al. 2023 examined SN 2020jfo), and these measurements are not all in agreement. Roy et al. (2011) used the standardized candle method to estimate a weighted mean distance of 13.19 ± 1.09 Mpc from mid-plateau apparent V -band magnitude, I -band magnitude, and photospheric velocity. Rodríguez et al.

(2014) find some of the largest distances by fitting photospheric magnitude diagrams, yielding distance measurements of 19.3 – 20.7 Mpc for NGC 4303. Bose & Kumar (2014) used two different models to derive distances with the expanding photosphere method (Hamuy et al. 2001; Dessart & Hillier 2005), and they find that these models differ by 30 – 50% across their sample. Pejcha & Prieto (2015) used a variation on the expanding photosphere method, and their resulting distance for NGC 4303 of $D = 18.73 \pm 5.57$ Mpc has a much greater uncertainty than other SNe II methods. However, recent progress has been made in standardizing SNe IIP (e.g., de Jaeger et al. 2022); in particular, Csörnyei et al. (2023) produced consistent results using two SNe IIP in NGC 4303. They used the spectral-fitting method introduced by Vogl et al. (2020), which takes a set of input parameters and predicts SNe IIP spectra. Applying this method to both SN 2008in and SN 2020jfo, they determined distances of $D = 15.06 \pm 0.71$ Mpc and $D = 14.95 \pm 0.78$ Mpc, respectively. These two distance measurements agree remarkably well, and the distance derived using SN 2008in is 2σ away from our distance measurement of $D = 16.47 \pm 0.27$ Mpc.

One distance often assumed for NGC 4303 comes from a group average presented in Kourkchi & Tully (2017) using distances listed in Tully et al. (2016) rather than a direct measurement of NGC 4303. Tully et al. (2016) reported NGC 4303 as one of a 39-member group, where 18 members have reported distances that span the range 25.35 – 52.72 Mpc with a group average distance reported as 33 Mpc. Kourkchi & Tully (2017) redefined galaxy groups within 3500 km s^{-1} and adopted a weighted group average of 16.99 ± 3.04 Mpc for NGC 4303, based on a new group that includes ten members with five distances reported spanning 16.00 – 26.30 Mpc.

Recently, Scheuermann et al. (2022) determined a distance of $13.49_{-1.60}^{+0.64}$ Mpc for NGC 4303 using PHANGS-MUSE data with the planetary nebula luminosity function (PNLF). Their findings highlight the potential effects of supernova remnant (SNR) contamination on PNLF distances. They classified 19 sources in NGC 4303 as planetary nebulae (PNe) and an additional eight sources as SNR. The inclusion of seven out of eight SNR (with the brightest source rejected) improved the fit of the PNLF, however these authors note that the inclusion of all eight SNR yielded a distance that was nearly 3 Mpc closer. Anand et al. (2021), also using PHANGS-MUSE data, employed the TRGB method to find distances to several PHANGS galaxies. However, they were unsuccessful in determining a distance to NGC 4303 using this method. They report that either an issue of depth be-

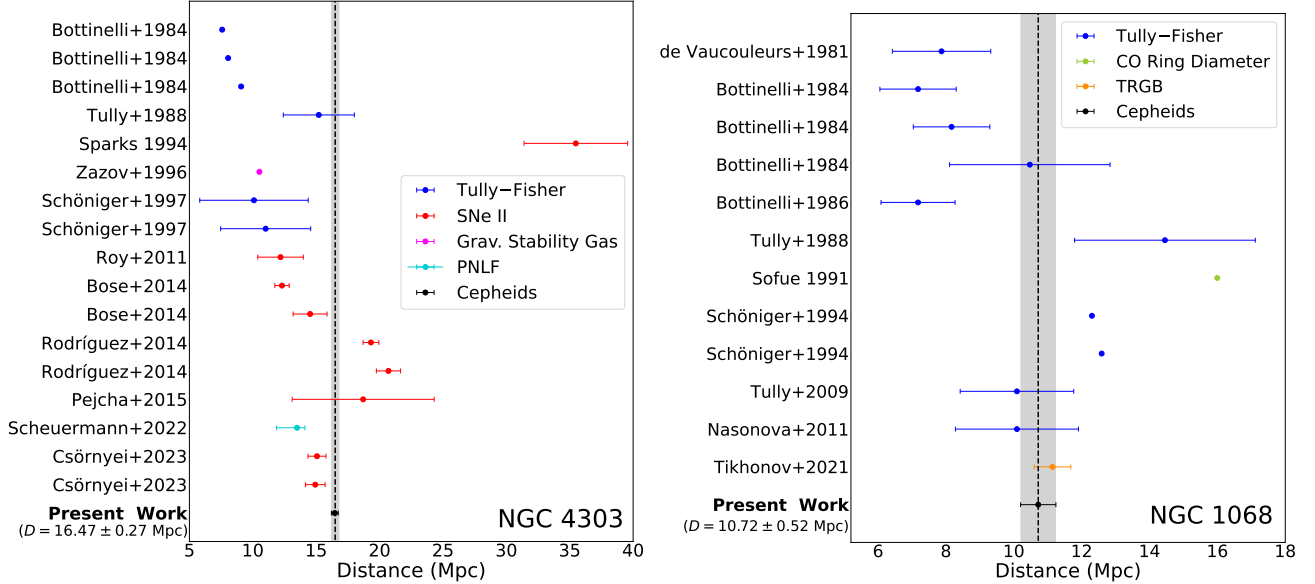


Figure 7. Comparison of previous distance measurements against our Cepheid-based distances for NGC 4303 (left) and NGC 1068 (right). Distance measurements are colored by their corresponding method. Multiple entries by the same authors coincide with multiple distance measurements reported in a single study. The vertical dashed lines represents our distance measurements, and the gray regions delimit our uncertainties.

low the TRGB or a lack of resolved sources in their chosen field limit their ability to constrain distances to some galaxies in their sample, including NGC 4303. This conclusion is supported by our distance measurement of $D = 16.47 \pm 0.27$ Mpc, as a distance of $D \gtrsim 15$ Mpc would likely explain an insufficient depth in the PHANGS data for constraining the TRGB.

In the case of NGC 1068, the redshift is often quoted instead of a distance measurement ($z = 0.003793$, de Vaucouleurs et al. 1991), though redshift-independent distance measurements do exist. Reported distances span 7.18 Mpc using the Tully–Fisher method (Bottinelli et al. 1984) to 16.0 Mpc using CO emission from the central ring of molecular gas (Sofue 1991, see Figure 7). The majority of distance measurements for NGC 1068 have been obtained using the Tully–Fisher method, though studies find a factor of ~ 2 spread in measurements using this method (7.18 – 14.4 Mpc, Bottinelli et al. 1984, 1986; Tully & Fisher 1988; Schöniger & Sofue 1994). NGC 1068 is moderately inclined ($i = 40 \pm 3^\circ$, Brinks et al. 1997), but it also has a more powerful AGN that could potentially impact Tully–Fisher results. The most recent distance measurement using the Tully–Fisher method is 10.1 ± 2.0 Mpc (Tully et al. 2009; Nasonova et al. 2011).

Other distances include $D = 11.14 \pm 0.54$ Mpc based on the Numerical Action Methods (NAM) of Shaya et al. (2017) and Kourkchi et al. (2020), though it is important to note that this distance is a model-based estimate rather than a measurement. Like NGC 4303, a TRGB

method distance measurement has also been attempted for NGC 1068. Tikhonov & Galazutdinova (2021) find a distance of 11.14 ± 0.54 Mpc using archival *HST* data in the F606W and F814W filters. However, the fields of the observations in the two filters do not overlap, and these authors consequently adopt an average $V - I$ color for metal-poor red giants ($V - I = 1.4 \pm 0.1$ mag). Our Cepheid-based distance measurement of $D = 10.72 \pm 0.52$ Mpc agrees fairly well with this TRGB measurement.

5.2. Peculiar Velocities and Environment

One open question regarding NGC 4303 is its association (or lack thereof) with the Virgo cluster. This galaxy cluster is expansive on the sky, and it is composed of several substructures that are distinct in their mean recessional velocities (e.g., Binggeli et al. 1985). Cantiello et al. (2024) recently produced a three-dimensional distribution of galaxies in the Virgo cluster using surface brightness fluctuation (SBF) distances. Our distance measurement to NGC 4303 is closest to the median distance of cluster B (Binggeli et al. 1993), though its position on the sky is significantly ($> 2^\circ$) outside of the cluster B radius, as defined by Boselli et al. (2014). There are southern cloud-like substructures closer to the position of NGC 4303 on the sky, and Binggeli et al. (1993) placed NGC 4303 as a member of the W cloud substructure. However, the average distances of these associations determined by Cantiello et al. (2024) are 22.7–29.0 Mpc, which is located behind NGC 4303. Karachentsev

& Nasonova (2013) characterize the dimensions of the Southern Extension, which they describe as a sheet with a depth of ~ 15 Mpc and a median distance of 17 ± 2 Mpc. Yoon et al. (2012) find evidence for a connective filament between the Southern Extension, W cloud, and M cloud. By examining Ly α absorption in and surrounding the Virgo cluster, they suggest the presence of a large-scale (> 3.6 Mpc) flow of warm gas. Based on our distance measurement and the location of NGC 4303 on the sky, it seems most likely that it is associated with either the Southern Extension or this connective filament.

To further investigate the association of NGC 4303 with the Virgo cluster, we determined the peculiar velocities affecting this galaxy. An H I recessional velocity of 1566 km s^{-1} is provided by Haynes et al. (2018). Adopting $H_0 = 73 \text{ km s}^{-1} \text{ Mpc}^{-1}$ (Riess et al. 2022) predicts a distance of $D = 21.5$ Mpc. Compared with our Cepheid-based distance, the redshift implies peculiar velocities of $\sim 300 - 400 \text{ km s}^{-1}$. A distance of $D = 16.47 \pm 0.27$ Mpc is similar to the average distances of both the Virgo cluster and the Southern Extension, though NGC 4303 appears to be moving away at a fairly high rate.

We also determined the peculiar velocities affecting NGC 1068. Bottinelli et al. (1990) report an H I recessional velocity of 1137 km s^{-1} . Once again adopting $H_0 = 73 \text{ km s}^{-1} \text{ Mpc}^{-1}$ (Riess et al. 2022), we obtain a distance of $D = 15.6$ Mpc. Similar to NGC 4303, we found peculiar velocities of $\sim 300 - 400 \text{ km s}^{-1}$ affecting NGC 1068. While NGC 1068 is not associated with a nearby massive galaxy cluster like the Virgo or Fornax clusters, Kourkchi & Tully (2017) determined it to be a part of a nine-member group. Two of the nine members have distances reported ($D = 19.41$ Mpc for NGC 1055, $D = 14.00$ Mpc for NGC 1087). The peculiar velocities affecting NGC 1068 may be related to its proximity to other massive galaxies.

Tully et al. (2013) have shown that peculiar velocities for nearby galaxies can reach $\sim 500 \text{ km s}^{-1}$, and it is not unusual for galaxies in groups to have peculiar velocities on the order of several 100 km s^{-1} . As is evident from both galaxies in our sample, redshift alone is not sufficient to derive accurate distances to nearby AGN.

5.3. Implications of New Distance Measurements

Considering the effect of our distance measurement on the black hole mass, a Cepheid-based distance of $D = 16.47 \pm 0.27$ Mpc for NGC 4303 agrees fairly well with the distance adopted by Pastorini et al. (2007) ($D = 16.1$ Mpc). Therefore, the central black hole mass they derive ($M_{\text{BH}} = 5.0_{-2.3}^{+0.9} \times 10^6 M_{\odot}$) is consistent within the given uncertainties. In their studies on the starburst–AGN connection, Riffel et al. (2016)

and Dametto et al. (2019) adopt the same distance of $D = 16.1$ Mpc. The size of the circumnuclear star-forming ring depends linearly on distance while the star formation rate (using Kennicutt 1998) and the masses of hot molecular and ionized gas inside the ring depend on distance squared. The findings of Riffel et al. (2016) and Dametto et al. (2019) are changed by $< 5\%$ by adopting our Cepheid-based distance. The luminosity of the nuclear region of NGC 4303 is dominated by star formation activity with weak contribution from a low-luminosity AGN (Colina et al. 2002; Jiménez-Bailón et al. 2003). The UV and X-ray luminosities determined by these authors ($\sim 10^{39} \text{ erg s}^{-1}$) also assume a distance of $D = 16.1$ Mpc, so these values remain relatively unchanged as well.

There are, however, several studies that have adopted quite different distances to NGC 4303. Davis et al. (2019) examined the SMBH mass (M_{BH})–bulge stellar mass ($M_{*,\text{sph}}$) scaling relation with a sample of spiral galaxies. They assumed a distance of $D = 12.3 \pm 0.6$ Mpc for NGC 4303, which is a factor of ~ 1.3 times smaller than our distance of $D = 16.47 \pm 0.27$ Mpc. Taking the stellar mass $M_{*,\text{sph}}$ from a mass-to-light ratio, their $M_{*,\text{sph}}$ value for NGC 4303 is ~ 1.7 times smaller than would be implied by our new distance. Graham & Sahu (2023) presented an updated $M_{\text{BH}} - M_{*,\text{sph}}$ scaling relation with a larger sample, and in this study, a distance of $D = 19.3 \pm 0.6$ was assumed for NGC 4303 (~ 1.2 times greater than our distance). In this case, the $M_{*,\text{sph}}$ value for NGC 4303 is ~ 1.4 times greater than what would be implied from our new distance measurement of $D = 16.47 \pm 0.27$ Mpc. An accurate distance for NGC 4303 thus has implications beyond the individual galaxy properties because it has the potential to also impact broader scaling relations.

The many different distances that have been adopted for NGC 1068 affect the results of several previous studies. Our Cepheid-based distance measurement of $D = 10.72 \pm 0.52$ Mpc for NGC 1068 is quite a bit smaller than the Tully–Fisher measurement of $D = 14.4$ Mpc (Tully & Fisher 1988); the two differ by a factor of ~ 1.3 . Lodato & Bertin (2003) derive a black hole mass of $M_{\text{BH}} = 8.0 \pm 0.3 \times 10^6 M_{\odot}$ for NGC 1068, assuming $D = 14.4$ Mpc. Scaling linearly with distance, our Cepheid-based measurement implies a mass closer to $\sim 6 \times 10^6 M_{\odot}$. Several studies of the kinematics and structure of gas in the torus of NGC 1068 (e.g., García-Burillo et al. 2014; Gámez Rosas et al. 2025) also assume a distance of 14.4 Mpc, which affects both the AGN luminosity and the reported scale of the outflows. García-Burillo et al. (2014) derived an AGN bolometric luminosity of $4.2_{-1.1}^{+1.4} \times 10^{44} \text{ erg s}^{-1}$, estimated from

CLUMPY model fits to the nuclear SED of NGC 1068. Gámez Rosas et al. (2025) assumed an AGN bolometric luminosity of $(0.4 - 4.7) \times 10^{45} \text{ erg s}^{-1}$, from GRAVITY Collaboration et al. (2020). Our distance measurement of $D = 10.72 \pm 0.52 \text{ Mpc}$ implies an AGN luminosity that is nearly a factor of 2 smaller than the values reported by these authors.

Some authors have adopted a redshift rather than a distance measurement for NGC 1068. Spinoglio et al. (2005) quoted a redshift of $z = 0.0038$ and corresponding distance of $D = 15.2 \text{ Mpc}$ (assuming $H_0 = 75 \text{ km s}^{-1} \text{ Mpc}^{-1}$) in their study of the far-infrared spectrum of NGC 1068. This distance is ~ 1.4 times larger than our distance measurement, and inaccurate line luminosities yield inaccuracies in the input physical parameters of models that are fit to the SED. In their study of the X-ray spectrum, Kamenetzky et al. (2011) assumed $H_0 = 70 \text{ km s}^{-1} \text{ Mpc}^{-1}$ for the same redshift ($z = 0.0038$), and this implies a distance of $D = 16.2 \text{ Mpc}$. Their angular size scale is ~ 1.5 larger than what is implied by our distance measurement of $D = 10.72 \pm 0.52$. The importance of an accurate distance measurement for NGC 1068 is evident in all wavelength regimes.

6. SUMMARY

We obtained multi-epoch HST imaging to identify and characterize Cepheid candidates in two canonical AGN host galaxies—NGC 4303 and NGC 1068. For each sample of Cepheid candidates, we fit the extinction-free W_I period–luminosity relationship to derive distance moduli. Carefully considering the potential effects of metallicity, we find $\mu = 31.083 \pm 0.035 \text{ mag}$ for NGC 4303 and $\mu = 30.150 \pm 0.106 \text{ mag}$ for NGC 1068. These correspond to distances of $D = 16.47 \pm 0.27 \text{ Mpc}$ and $D = 10.72 \pm 0.52 \text{ Mpc}$, respectively.

Our Cepheid-based distance to NGC 4303 agrees fairly well with the distance commonly used to determine its black hole mass and nuclear luminosity ($D = 16.1 \text{ Mpc}$). Therefore, these characteristics are relatively unaffected by our new distance measurement. However, other work

that adopted different distances will be affected, including studies of scaling relations such as the $M_{BH} - M_{*,sph}$ relationship. Our distance to NGC 1068 differs from the often adopted $D = 14.4 \text{ Mpc}$ by a factor of ~ 1.3 . This implies a factor of ~ 1.3 decrease in central black hole mass and a factor of ~ 1.7 decrease in AGN luminosity measurements. Our distance measurements for both NGC 4303 and NGC 1068 imply peculiar velocities of $\sim 300 - 400 \text{ km s}^{-1}$, which demonstrates that redshift alone is insufficient for estimating their distances.

ACKNOWLEDGMENTS

We thank the referee for their helpful suggestions. We thank Judy Schmidt for her production of the images displayed in Figure 1. M. Markham thanks Eugene Vasiliev for his constructive comments. We thank D. Michael Crenshaw and Monica Valluri for their contributions to the proposal. M. Markham and M.C. Bentz gratefully acknowledge support through program HST GO-17165, which was provided by NASA through a grant from the Space Telescope Science Institute, which is operated by the Association of Universities for Research in Astronomy, Inc., under NASA contract NAS 5-26555. M. Vestergaard gratefully acknowledges financial support from the Independent Research Fund Denmark via grant number DFF 3103-00146 and from the Carlsberg Foundation (grant CF23-0417).

AUTHOR CONTRIBUTIONS

M. Markham drizzled the observations, carried out the analysis, and wrote the manuscript. M.C. Bentz led the proposal and Phase 2 planning and oversaw the project. L. Ferrarese, C.A. Onken, and M. Vestergaard provided scientific expertise. All authors contributed to the presentation of the results.

Facility: HST (WFC3)

Software: AstroDrizzle (Fruchter et al. 2010), DAOPHOT (Stetson 1987)

APPENDIX

A. NGC 4303

The Cepheid candidates in Table 3 and Figure 8 represent our final 3σ -clipped sample in NGC 4303. Sources with periods below our visually-determined point of completeness ($P > 19.5 \text{ days}$) are included here.

Table 3. Best-fit Light Curve Parameters for Final Cepheid Candidates in NGC 4303

ID	RA (hh:mm:ss)	Dec (dd:mm:ss)	m_{F555W} (mag)	m_{F814W} (mag)	P (days)	Phase (days)	χ^2/ν
1	12:21:53.263	+04:27:03.486	25.98 ± 0.08	26.76 ± 0.04	13.17 ± 0.17	12.00 ± 0.32	1.35
2	12:21:53.468	+04:27:16.826	25.39 ± 0.05	26.28 ± 0.04	15.83 ± 0.21	4.56 ± 0.37	1.73
3	12:21:51.230	+04:27:21.124	25.85 ± 0.05	26.95 ± 0.03	15.82 ± 0.21	7.26 ± 0.47	1.28
4	12:21:56.212	+04:27:10.250	25.62 ± 0.04	26.17 ± 0.02	16.66 ± 0.18	6.31 ± 0.40	1.13
5	12:21:54.775	+04:27:35.278	25.18 ± 0.05	26.05 ± 0.03	17.42 ± 0.36	11.70 ± 0.39	1.15
6	12:21:52.141	+04:28:19.510	25.43 ± 0.04	26.35 ± 0.02	18.68 ± 0.10	5.21 ± 0.23	0.77
7	12:21:57.700	+04:28:54.315	25.10 ± 0.05	25.81 ± 0.03	20.01 ± 0.48	8.70 ± 0.50	2.62
8	12:21:56.455	+04:28:50.334	25.16 ± 0.06	26.14 ± 0.04	20.38 ± 0.14	9.64 ± 0.25	2.09
9	12:21:57.615	+04:27:56.948	25.10 ± 0.04	25.76 ± 0.03	20.69 ± 0.45	14.02 ± 0.63	1.66
10	12:21:51.716	+04:27:10.241	25.50 ± 0.06	26.46 ± 0.05	21.06 ± 0.69	15.49 ± 0.22	2.67
11	12:21:58.877	+04:27:49.639	25.75 ± 0.04	26.70 ± 0.02	21.28 ± 0.35	1.45 ± 0.67	0.72
12	12:21:50.588	+04:28:54.812	25.31 ± 0.07	26.27 ± 0.04	22.14 ± 0.37	3.45 ± 1.00	3.22
13	12:21:51.592	+04:28:06.725	24.95 ± 0.05	25.92 ± 0.03	22.49 ± 0.20	17.14 ± 0.28	1.71
14	12:21:53.282	+04:27:36.688	24.90 ± 0.05	25.75 ± 0.06	22.72 ± 0.53	14.01 ± 0.83	2.21
15	12:21:51.569	+04:29:18.385	25.50 ± 0.05	26.49 ± 0.03	22.82 ± 0.23	22.41 ± 0.26	2.06
16	12:21:50.933	+04:27:27.725	25.29 ± 0.07	26.72 ± 0.05	24.11 ± 0.82	8.50 ± 1.09	2.69
17	12:21:50.895	+04:29:12.196	24.76 ± 0.04	25.66 ± 0.02	24.34 ± 0.33	7.59 ± 0.36	1.34
18	12:21:54.962	+04:29:13.140	25.08 ± 0.04	25.78 ± 0.03	25.20 ± 0.39	11.97 ± 0.71	0.67
19	12:21:54.752	+04:27:31.321	25.32 ± 0.05	26.24 ± 0.05	26.14 ± 0.81	19.39 ± 1.07	2.24
20	12:21:56.100	+04:27:07.301	24.64 ± 0.03	25.48 ± 0.02	26.80 ± 0.40	5.63 ± 0.43	1.19
21	12:21:50.748	+04:28:48.214	24.90 ± 0.04	26.17 ± 0.03	27.12 ± 0.91	22.27 ± 0.30	1.73
22	12:21:54.770	+04:27:23.451	25.11 ± 0.07	26.03 ± 0.04	27.24 ± 0.62	25.26 ± 0.36	4.51
23	12:21:50.374	+04:29:07.801	24.90 ± 0.05	25.62 ± 0.03	27.54 ± 0.62	17.89 ± 0.52	4.36
24	12:21:50.941	+04:27:29.845	24.66 ± 0.05	25.73 ± 0.02	28.71 ± 0.80	1.95 ± 0.83	2.21
25	12:21:56.052	+04:28:07.481	24.43 ± 0.04	25.33 ± 0.03	28.91 ± 0.63	13.99 ± 0.32	2.22
26	12:21:59.113	+04:28:36.523	24.75 ± 0.05	25.53 ± 0.05	28.95 ± 0.74	12.96 ± 0.63	3.25
27	12:21:57.359	+04:29:23.384	24.69 ± 0.04	25.76 ± 0.03	29.22 ± 0.57	4.14 ± 0.97	2.10
28	12:21:52.683	+04:27:02.249	25.26 ± 0.03	26.31 ± 0.02	30.17 ± 0.22	11.33 ± 0.25	1.52
29	12:21:52.047	+04:27:28.152	24.73 ± 0.06	25.92 ± 0.05	31.36 ± 1.02	8.08 ± 0.88	4.68
30	12:21:53.750	+04:27:41.434	24.42 ± 0.05	25.54 ± 0.03	31.52 ± 0.50	12.16 ± 0.46	1.91
31	12:21:50.549	+04:28:47.959	25.41 ± 0.06	26.50 ± 0.04	31.59 ± 0.84	21.56 ± 0.29	2.95
32	12:21:53.049	+04:29:12.018	25.06 ± 0.02	26.14 ± 0.01	31.61 ± 0.23	21.20 ± 0.11	0.60
33	12:21:56.518	+04:28:27.730	24.41 ± 0.04	25.11 ± 0.02	32.35 ± 0.38	32.34 ± 0.25	1.34
34	12:21:50.573	+04:28:18.871	25.18 ± 0.04	26.27 ± 0.04	32.48 ± 0.69	7.25 ± 1.18	1.20
35	12:21:54.057	+04:29:21.817	24.89 ± 0.03	25.89 ± 0.03	32.75 ± 0.42	30.71 ± 0.20	1.04
36	12:21:50.121	+04:28:52.686	24.98 ± 0.03	26.06 ± 0.03	33.31 ± 0.75	21.93 ± 0.25	1.80
37	12:21:56.631	+04:27:31.086	24.49 ± 0.08	25.68 ± 0.08	34.03 ± 2.02	13.56 ± 2.51	7.42
38	12:21:50.106	+04:29:07.606	24.90 ± 0.04	26.10 ± 0.03	34.52 ± 0.92	21.23 ± 0.25	2.15
39	12:21:56.277	+04:28:24.736	24.33 ± 0.08	25.43 ± 0.05	34.59 ± 0.61	0.22 ± 0.81	4.40

Table 3 *continued*

Table 3 (continued)

ID	RA (hh:mm:ss)	Dec (dd:mm:ss)	m_{F555W} (mag)	m_{F814W} (mag)	P (days)	Phase (days)	χ^2/ν
40	12:21:52.636	+04:28:52.771	24.61 ± 0.05	25.60 ± 0.04	34.94 ± 1.26	12.85 ± 0.83	3.96
41	12:21:50.683	+04:28:53.698	24.67 ± 0.06	25.85 ± 0.04	34.97 ± 0.83	17.93 ± 0.62	5.92
42	12:21:57.362	+04:28:51.644	24.77 ± 0.05	25.74 ± 0.03	34.98 ± 0.66	11.27 ± 0.23	2.41
43	12:21:59.140	+04:28:00.798	25.10 ± 0.07	26.04 ± 0.06	35.14 ± 1.51	12.55 ± 1.57	5.22
44	12:21:53.705	+04:27:43.014	24.31 ± 0.06	25.11 ± 0.04	35.19 ± 1.20	12.36 ± 1.21	3.72
45	12:21:56.688	+04:29:32.895	24.73 ± 0.05	25.68 ± 0.04	35.68 ± 0.78	1.36 ± 0.68	2.12
46	12:21:59.724	+04:28:36.650	24.63 ± 0.05	25.63 ± 0.04	35.83 ± 1.52	19.85 ± 0.74	5.29
47	12:21:53.441	+04:29:03.488	24.70 ± 0.04	25.45 ± 0.02	35.89 ± 0.45	10.10 ± 0.24	2.29
48	12:21:56.183	+04:28:28.921	24.57 ± 0.05	25.48 ± 0.03	35.94 ± 0.55	0.96 ± 0.44	3.04
49	12:21:55.016	+04:27:29.317	24.54 ± 0.03	25.37 ± 0.02	36.17 ± 0.36	0.05 ± 0.32	1.65
50	12:21:56.566	+04:28:30.630	24.81 ± 0.05	25.89 ± 0.04	36.21 ± 1.13	18.16 ± 0.67	3.16
51	12:21:53.763	+04:29:33.005	24.33 ± 0.04	25.36 ± 0.03	36.61 ± 0.55	36.50 ± 0.48	4.71
52	12:21:49.586	+04:28:48.503	24.60 ± 0.05	25.60 ± 0.04	36.80 ± 1.90	28.66 ± 0.29	5.08
53	12:21:50.605	+04:28:45.944	24.69 ± 0.04	25.67 ± 0.03	37.57 ± 1.22	9.83 ± 0.35	2.88
54	12:21:59.140	+04:27:52.247	24.81 ± 0.05	25.78 ± 0.03	38.10 ± 1.12	10.38 ± 0.37	4.12
55	12:21:55.279	+04:27:05.601	24.75 ± 0.03	25.81 ± 0.02	38.15 ± 0.51	33.86 ± 0.36	1.36
56	12:21:55.686	+04:27:04.628	24.44 ± 0.04	25.32 ± 0.03	38.54 ± 0.66	10.97 ± 0.61	5.09
57	12:21:55.482	+04:29:17.255	24.45 ± 0.04	25.53 ± 0.02	38.64 ± 0.39	22.25 ± 0.25	1.77
58	12:21:54.900	+04:29:19.709	24.46 ± 0.03	25.32 ± 0.02	38.69 ± 0.77	2.34 ± 0.55	1.46
59	12:21:52.628	+04:29:12.704	24.68 ± 0.03	25.71 ± 0.02	39.00 ± 0.56	12.16 ± 0.43	3.06
60	12:21:56.313	+04:28:52.842	24.54 ± 0.02	25.70 ± 0.02	39.02 ± 0.43	23.39 ± 0.32	0.79
61	12:21:54.548	+04:27:41.062	24.82 ± 0.06	25.86 ± 0.04	39.15 ± 1.74	18.22 ± 0.57	3.57
62	12:21:53.587	+04:29:21.745	23.96 ± 0.06	24.76 ± 0.03	39.20 ± 0.42	30.37 ± 0.28	3.38
63	12:21:54.507	+04:27:01.090	24.81 ± 0.04	25.94 ± 0.03	39.32 ± 0.58	11.33 ± 0.40	4.37
64	12:21:52.913	+04:28:14.473	25.11 ± 0.07	26.64 ± 0.06	39.41 ± 1.07	11.44 ± 0.81	4.37
65	12:21:51.151	+04:28:46.942	24.28 ± 0.04	25.22 ± 0.03	39.45 ± 0.59	33.06 ± 0.31	3.82
66	12:21:51.061	+04:28:24.990	24.65 ± 0.07	25.78 ± 0.04	39.82 ± 1.09	12.88 ± 0.62	4.71
67	12:21:59.769	+04:28:23.270	24.91 ± 0.04	26.27 ± 0.04	39.83 ± 0.58	30.13 ± 0.32	1.82
68	12:21:55.910	+04:28:57.816	24.64 ± 0.04	25.80 ± 0.02	40.05 ± 0.51	11.95 ± 0.42	1.60
69	12:21:55.705	+04:29:28.256	24.36 ± 0.03	25.44 ± 0.05	40.92 ± 1.29	38.53 ± 1.19	2.26
70	12:21:51.805	+04:27:50.693	24.55 ± 0.04	25.57 ± 0.03	40.99 ± 0.84	40.31 ± 0.81	1.83
71	12:21:57.529	+04:29:32.191	24.85 ± 0.03	26.09 ± 0.02	41.29 ± 0.51	9.69 ± 0.39	1.25
72	12:21:55.556	+04:29:19.767	24.10 ± 0.04	25.19 ± 0.02	41.66 ± 0.54	21.46 ± 0.31	2.12
73	12:21:56.817	+04:27:11.465	24.38 ± 0.04	25.23 ± 0.03	42.56 ± 1.72	12.58 ± 1.62	7.63
74	12:21:52.736	+04:28:50.161	24.59 ± 0.04	25.74 ± 0.03	42.80 ± 1.28	24.40 ± 0.48	2.65
75	12:21:58.613	+04:28:07.594	24.63 ± 0.03	25.93 ± 0.02	42.97 ± 1.11	7.40 ± 0.41	1.50
76	12:21:55.808	+04:27:16.089	24.54 ± 0.04	25.66 ± 0.02	43.27 ± 1.00	23.75 ± 0.32	2.18
77	12:21:57.887	+04:28:08.721	24.43 ± 0.06	25.28 ± 0.04	43.48 ± 1.13	1.57 ± 0.72	5.73
78	12:21:50.141	+04:28:53.082	24.58 ± 0.03	25.78 ± 0.05	43.50 ± 1.31	38.05 ± 1.44	1.35
79	12:21:52.484	+04:27:27.753	24.49 ± 0.03	25.82 ± 0.03	43.49 ± 1.64	34.75 ± 0.68	2.16

Table 3 continued

Table 3 (continued)

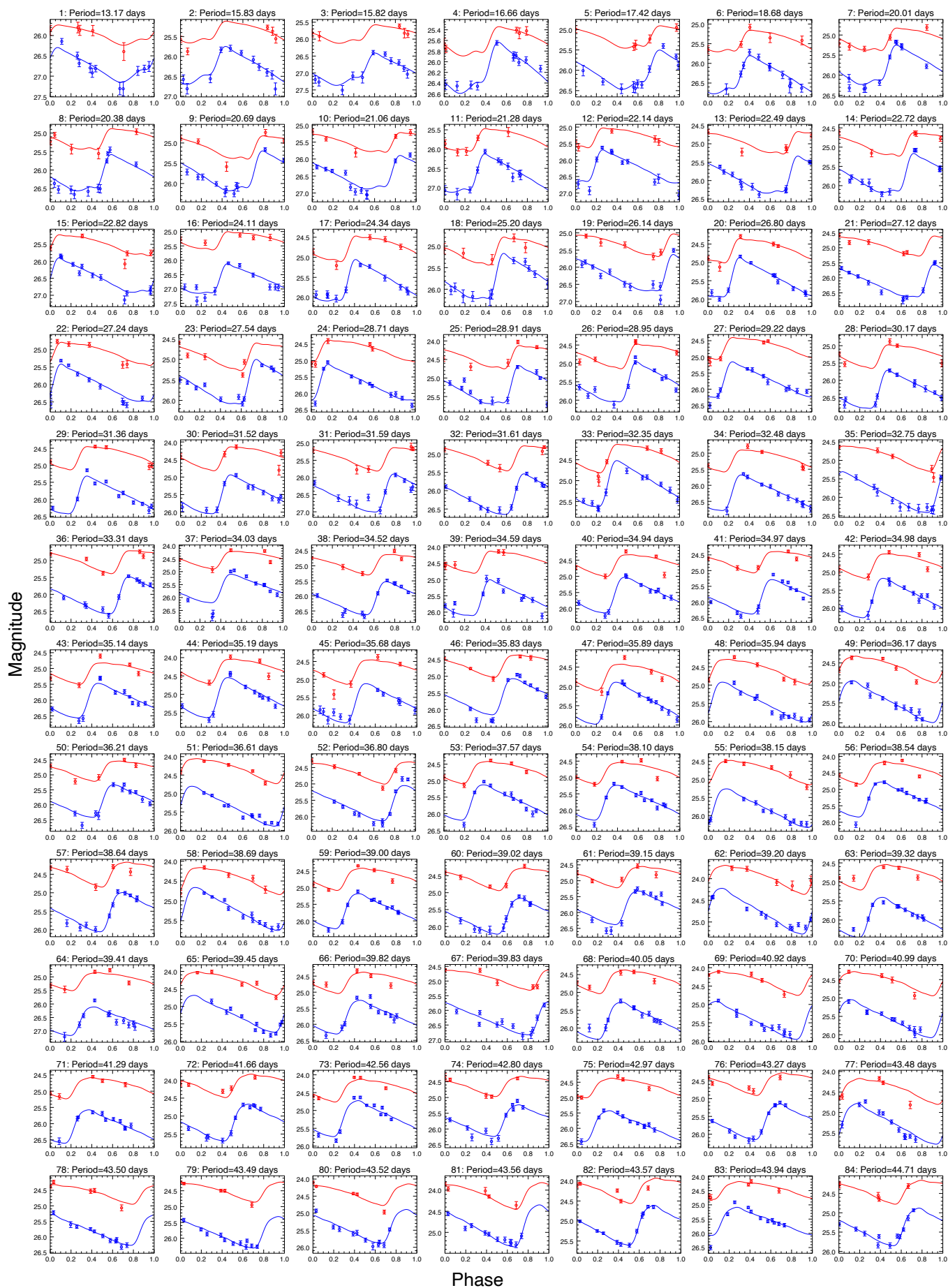
ID	RA (hh:mm:ss)	Dec (dd:mm:ss)	m_{F555W} (mag)	m_{F814W} (mag)	P (days)	Phase (days)	χ^2/ν
80	12:21:54.235	+04:27:31.145	24.40 ± 0.03	25.39 ± 0.04	43.52 ± 1.83	32.93 ± 0.39	3.48
81	12:21:52.656	+04:28:47.160	24.08 ± 0.03	24.85 ± 0.02	43.56 ± 1.32	33.36 ± 0.40	1.88
82	12:21:52.489	+04:27:18.968	24.19 ± 0.04	25.11 ± 0.02	43.57 ± 0.75	26.15 ± 0.33	3.54
83	12:21:50.639	+04:28:47.148	24.44 ± 0.09	25.58 ± 0.05	43.94 ± 3.11	5.83 ± 3.13	6.87
84	12:21:51.910	+04:28:43.069	24.41 ± 0.04	25.37 ± 0.03	44.71 ± 0.67	28.05 ± 0.34	2.53
85	12:21:58.158	+04:28:33.816	23.86 ± 0.05	24.80 ± 0.02	45.18 ± 1.53	30.21 ± 0.29	2.74
86	12:21:56.513	+04:29:08.928	24.41 ± 0.02	25.56 ± 0.01	46.44 ± 0.34	23.25 ± 0.21	0.51
87	12:21:58.755	+04:28:16.499	24.76 ± 0.06	25.77 ± 0.04	46.72 ± 1.20	16.48 ± 0.73	4.20
88	12:21:54.718	+04:29:15.019	24.11 ± 0.05	25.18 ± 0.03	46.86 ± 0.69	24.73 ± 0.41	1.62
89	12:21:58.007	+04:29:19.719	24.56 ± 0.04	25.74 ± 0.03	47.12 ± 1.34	2.97 ± 0.64	3.04
90	12:21:52.712	+04:28:35.593	24.36 ± 0.05	25.24 ± 0.03	47.15 ± 1.00	14.99 ± 0.57	3.39
91	12:21:56.523	+04:29:32.663	24.57 ± 0.04	26.03 ± 0.04	47.19 ± 2.64	39.09 ± 1.27	0.93
92	12:21:57.581	+04:27:53.402	24.17 ± 0.04	24.88 ± 0.02	47.52 ± 1.65	30.81 ± 0.31	2.33
93	12:21:56.088	+04:27:47.832	24.09 ± 0.03	25.16 ± 0.02	47.64 ± 0.72	0.52 ± 0.57	1.10
94	12:21:55.744	+04:28:44.518	23.80 ± 0.05	24.66 ± 0.03	49.20 ± 2.51	33.93 ± 0.61	4.55
95	12:21:50.541	+04:28:59.003	24.11 ± 0.03	24.96 ± 0.02	49.60 ± 1.59	5.33 ± 1.31	1.81
96	12:21:52.856	+04:29:27.773	24.66 ± 0.04	25.76 ± 0.03	49.96 ± 1.32	19.27 ± 1.29	4.75
97	12:21:55.531	+04:29:17.019	23.96 ± 0.04	25.06 ± 0.02	50.63 ± 0.79	22.16 ± 0.47	2.90
98	12:21:51.393	+04:29:02.296	24.44 ± 0.03	25.88 ± 0.03	50.91 ± 2.28	47.21 ± 0.70	3.21
99	12:21:55.671	+04:27:05.050	24.05 ± 0.04	25.04 ± 0.03	51.08 ± 1.37	13.83 ± 1.25	6.62
100	12:21:56.226	+04:27:01.319	24.26 ± 0.05	25.31 ± 0.03	51.11 ± 1.36	13.41 ± 0.86	6.60
101	12:21:55.499	+04:29:25.395	23.98 ± 0.03	24.83 ± 0.02	51.51 ± 1.31	6.43 ± 0.70	1.68
102	12:21:56.974	+04:27:27.397	24.15 ± 0.04	25.22 ± 0.03	51.57 ± 1.52	14.54 ± 0.84	4.41
103	12:21:59.145	+04:27:42.283	23.94 ± 0.04	24.94 ± 0.03	51.67 ± 1.80	26.00 ± 0.65	4.74
104	12:21:53.615	+04:27:29.220	24.01 ± 0.02	24.95 ± 0.02	52.29 ± 1.44	35.50 ± 0.55	1.48
105	12:21:54.358	+04:27:03.507	24.79 ± 0.04	26.19 ± 0.04	52.99 ± 3.23	45.74 ± 0.74	3.18
106	12:21:56.117	+04:29:26.505	24.14 ± 0.02	25.23 ± 0.02	53.38 ± 1.60	43.05 ± 0.51	0.56
107	12:21:52.120	+04:27:52.187	24.05 ± 0.04	25.16 ± 0.03	54.21 ± 1.78	53.03 ± 0.89	3.64
108	12:21:53.663	+04:29:30.160	24.65 ± 0.04	25.92 ± 0.03	55.56 ± 3.33	46.16 ± 0.68	3.08
109	12:21:51.271	+04:28:56.140	24.25 ± 0.06	25.32 ± 0.05	55.73 ± 5.37	46.57 ± 1.13	10.59
110	12:21:50.271	+04:29:02.666	24.49 ± 0.05	25.90 ± 0.04	56.55 ± 3.68	51.43 ± 1.09	2.70
111	12:21:57.544	+04:28:41.058	23.91 ± 0.03	24.98 ± 0.02	56.65 ± 2.30	39.83 ± 1.11	1.10
112	12:21:51.132	+04:29:16.979	24.18 ± 0.02	25.48 ± 0.02	56.98 ± 1.30	54.46 ± 0.61	1.08
113	12:21:56.959	+04:27:44.300	24.10 ± 0.04	25.32 ± 0.03	59.34 ± 2.35	22.43 ± 1.09	2.56
114	12:21:53.501	+04:29:33.899	23.74 ± 0.04	24.99 ± 0.02	61.02 ± 2.57	4.30 ± 1.82	1.56
115	12:21:58.834	+04:27:58.165	24.77 ± 0.03	26.15 ± 0.03	61.55 ± 3.39	29.78 ± 0.67	1.97
116	12:21:56.025	+04:29:21.437	23.89 ± 0.03	24.93 ± 0.03	61.72 ± 3.95	50.63 ± 1.22	2.99
117	12:21:55.324	+04:29:27.332	23.71 ± 0.03	24.53 ± 0.02	61.77 ± 2.14	50.29 ± 0.71	2.63
118	12:21:50.569	+04:28:34.755	24.04 ± 0.04	25.49 ± 0.03	63.35 ± 2.36	0.81 ± 1.76	3.43
119	12:21:53.061	+04:29:20.687	23.68 ± 0.03	24.59 ± 0.03	63.43 ± 2.83	34.48 ± 0.91	5.09

Table 3 continued

Table 3 (*continued*)

ID	RA (hh:mm:ss)	Dec (dd:mm:ss)	m_{F555W} (mag)	m_{F814W} (mag)	P (days)	Phase (days)	χ^2/ν
120	12:21:58.081	+04:28:26.644	23.83 ± 0.03	24.69 ± 0.02	64.00 ± 1.65	22.85 ± 1.57	1.17
121	12:21:55.285	+04:27:06.767	23.47 ± 0.05	24.55 ± 0.01	65.92 ± 1.94	35.64 ± 0.87	1.52
122	12:21:49.717	+04:28:45.428	23.68 ± 0.04	24.83 ± 0.04	66.05 ± 8.39	46.29 ± 1.84	8.02
123	12:21:54.567	+04:29:29.406	23.56 ± 0.03	24.54 ± 0.03	66.50 ± 4.13	50.10 ± 1.31	5.23
124	12:21:55.068	+04:29:12.310	23.99 ± 0.03	25.03 ± 0.02	68.17 ± 3.81	53.78 ± 1.10	1.83
125	12:21:51.227	+04:27:25.572	23.72 ± 0.02	25.17 ± 0.02	73.32 ± 4.28	62.94 ± 1.19	1.21
126	12:21:56.383	+04:29:20.021	24.01 ± 0.04	25.24 ± 0.04	75.69 ± 7.39	27.88 ± 1.59	3.35
127	12:21:56.170	+04:29:29.822	23.24 ± 0.04	24.00 ± 0.02	77.92 ± 7.27	38.20 ± 2.08	3.12
128	12:21:58.194	+04:28:33.806	22.90 ± 0.03	23.96 ± 0.03	86.31 ± 8.39	75.34 ± 3.27	3.42
129	12:21:57.199	+04:27:53.671	22.93 ± 0.03	23.78 ± 0.02	86.48 ± 6.66	29.58 ± 1.32	2.59
130	12:21:56.431	+04:28:49.211	23.68 ± 0.01	24.87 ± 0.02	93.27 ± 4.33	19.15 ± 0.97	0.45

NOTE—The ID's of each Cepheid candidate correspond to the ID's of each light curve in Figure 8. The phases here are given in days with respect to the first visit. χ^2/ν is the reduced χ^2 value for the F555W Cepheid template fit.



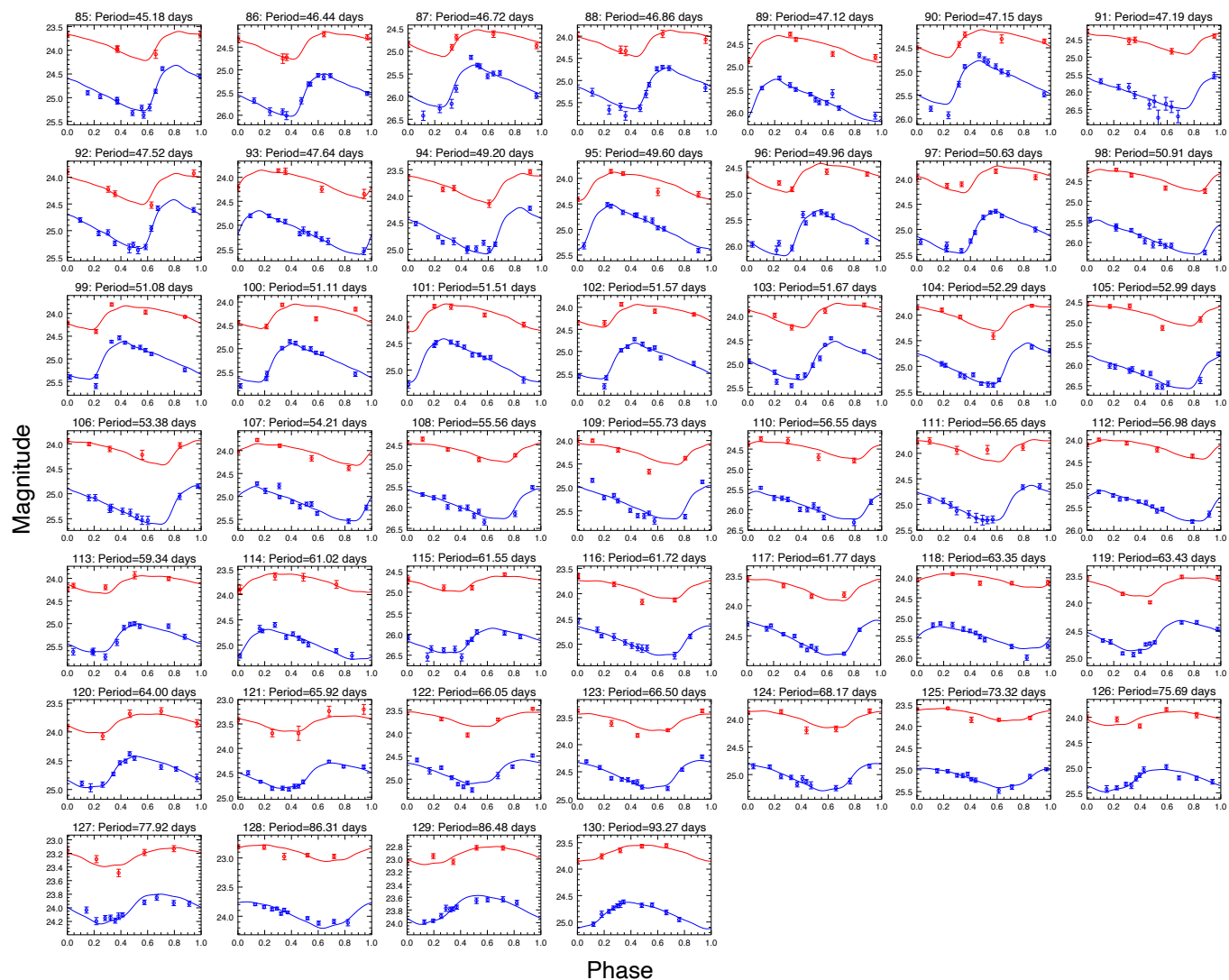


Figure 8. Light curves for 130 final Cepheid candidates in NGC 4303. The data points show the measurements in F555W (blue) and F814W (red), while the solid lines represent the best Cepheid template fits to the data.

B. NGC 1068

As in Section A, the Cepheid candidates in Table 4 and Figure 9 represent our final 3σ -clipped sample for NGC 1068. Sources with periods below the point of completeness ($P > 25$ days, as determined by Figure 6) are also included.

Table 4. Best-fit Light Curve Parameters for Final Cepheid Candidates in NGC 1068

ID	RA (hh:mm:ss)	Dec (dd:mm:ss)	m_{F555W} (mag)	m_{F814W} (mag)	P (days)	Phase (days)	χ^2/ν
1	02:42:43.828	-00:01:27.473	25.72 ± 0.07	26.83 ± 0.04	13.70 ± 0.27	3.13 ± 0.94	1.48
2	02:42:41.336	-00:01:26.882	25.02 ± 0.06	26.15 ± 0.03	13.89 ± 0.11	11.13 ± 0.35	1.26
3	02:42:46.415	-00:01:18.621	25.88 ± 0.09	26.57 ± 0.07	15.71 ± 0.39	11.02 ± 1.07	5.22
4	02:42:40.588	-00:01:36.045	25.61 ± 0.07	27.47 ± 0.06	16.34 ± 0.39	9.14 ± 1.03	1.04
5	02:42:41.153	-00:01:22.600	25.07 ± 0.04	26.28 ± 0.03	17.39 ± 0.24	4.06 ± 0.45	0.55
6	02:42:41.220	-00:00:01.335	24.86 ± 0.07	25.93 ± 0.04	18.32 ± 0.50	13.31 ± 0.58	3.02
7	02:42:42.910	-00:00:24.682	24.98 ± 0.06	26.19 ± 0.05	18.92 ± 0.43	14.59 ± 0.79	2.25
8	02:42:38.743	-00:01:10.896	24.47 ± 0.05	25.62 ± 0.05	19.29 ± 0.43	14.25 ± 0.84	1.50
9	02:42:38.895	-00:00:03.623	24.51 ± 0.06	25.67 ± 0.04	19.43 ± 0.35	7.77 ± 0.93	4.41
10	02:42:41.015	-00:01:48.774	25.55 ± 0.06	26.69 ± 0.04	19.73 ± 0.34	12.57 ± 0.43	1.34
11	02:42:44.100	-00:01:23.543	25.08 ± 0.10	26.17 ± 0.05	20.00 ± 0.28	10.42 ± 0.53	6.73
12	02:42:45.499	-00:00:15.180	25.41 ± 0.05	26.08 ± 0.05	23.12 ± 0.44	11.02 ± 1.03	2.70
13	02:42:43.513	-00:01:32.601	25.81 ± 0.06	27.68 ± 0.05	24.41 ± 0.73	8.83 ± 1.19	0.74
14	02:42:41.467	-00:01:34.264	24.26 ± 0.06	26.20 ± 0.05	26.56 ± 0.80	7.22 ± 1.35	2.10
15	02:42:44.531	-00:00:38.679	25.02 ± 0.04	26.40 ± 0.03	27.51 ± 0.64	22.38 ± 0.51	1.10
16	02:42:43.356	-00:00:22.337	24.53 ± 0.05	25.89 ± 0.04	30.30 ± 0.48	21.65 ± 0.34	3.29
17	02:42:41.198	-00:00:01.252	24.28 ± 0.05	25.53 ± 0.04	30.66 ± 0.56	21.67 ± 0.46	2.33
18	02:42:42.961	-00:00:39.990	24.36 ± 0.06	25.69 ± 0.04	31.70 ± 0.93	27.84 ± 0.87	2.68
19	02:42:39.105	-00:01:09.252	24.05 ± 0.05	25.50 ± 0.04	32.95 ± 1.18	12.39 ± 1.11	2.43
20	02:42:39.463	-00:01:05.191	24.06 ± 0.07	25.18 ± 0.03	33.02 ± 0.52	26.37 ± 0.39	3.50
21	02:42:40.112	-00:00:11.071	24.11 ± 0.06	25.61 ± 0.04	33.16 ± 1.19	11.82 ± 1.16	4.03
22	02:42:41.460	-00:01:24.792	24.02 ± 0.07	25.29 ± 0.04	33.40 ± 1.15	28.13 ± 0.91	4.28
23	02:42:43.068	-00:00:39.695	24.09 ± 0.06	25.44 ± 0.03	33.99 ± 1.10	10.52 ± 1.08	3.00
24	02:42:43.172	-00:00:42.286	24.76 ± 0.10	26.13 ± 0.07	34.13 ± 0.56	31.89 ± 0.47	3.85
25	02:42:40.611	-00:01:44.783	24.13 ± 0.06	25.66 ± 0.04	34.95 ± 0.46	32.29 ± 0.31	3.88
26	02:42:38.892	-00:01:25.492	24.62 ± 0.06	26.07 ± 0.05	35.53 ± 1.56	10.53 ± 0.66	2.62
27	02:42:43.261	-00:00:28.701	24.09 ± 0.04	25.22 ± 0.03	37.02 ± 0.70	27.51 ± 0.63	3.37
28	02:42:38.670	-00:01:03.271	23.91 ± 0.05	25.40 ± 0.04	38.91 ± 1.02	33.07 ± 0.39	1.97
29	02:42:38.017	-00:00:04.772	24.08 ± 0.06	25.45 ± 0.05	39.26 ± 1.62	15.09 ± 1.10	7.77
30	02:42:38.762	-00:00:40.367	24.02 ± 0.06	25.70 ± 0.04	39.95 ± 1.58	11.79 ± 1.65	2.03
31	02:42:36.887	-00:00:38.555	25.39 ± 0.07	27.35 ± 0.07	40.86 ± 1.52	2.11 ± 1.41	1.76
32	02:42:40.861	-00:01:11.386	23.79 ± 0.06	25.77 ± 0.06	46.39 ± 1.93	25.45 ± 1.17	4.12
33	02:42:41.435	-00:01:27.152	23.16 ± 0.03	24.61 ± 0.02	47.58 ± 1.42	30.73 ± 0.29	1.35
34	02:42:41.112	-00:01:06.934	23.75 ± 0.05	25.50 ± 0.04	49.00 ± 1.19	1.95 ± 0.75	2.00
35	02:42:43.640	-00:00:26.371	23.63 ± 0.02	24.68 ± 0.02	51.98 ± 1.31	32.00 ± 0.27	1.21

Table 4 *continued*

Table 4 (*continued*)

ID	RA (hh:mm:ss)	Dec (dd:mm:ss)	m_{F555W} (mag)	m_{F814W} (mag)	P (days)	Phase (days)	χ^2/ν
36	02:42:38.483	-00:01:07.884	23.38 ± 0.06	24.90 ± 0.05	53.40 ± 2.80	20.46 ± 1.24	12.05
37	02:42:41.379	-00:00:09.759	24.02 ± 0.05	25.64 ± 0.03	56.23 ± 2.46	22.46 ± 0.84	2.58
38	02:42:43.481	-00:00:22.368	23.71 ± 0.04	25.12 ± 0.03	59.10 ± 3.67	49.50 ± 1.86	3.21
39	02:42:41.059	-00:01:23.397	23.25 ± 0.04	25.15 ± 0.04	60.72 ± 4.38	16.88 ± 1.79	1.93
40	02:42:39.462	-00:01:38.151	23.86 ± 0.04	25.64 ± 0.03	62.56 ± 1.74	61.65 ± 1.09	2.43
41	02:42:41.061	-00:00:01.724	23.08 ± 0.03	24.53 ± 0.02	63.69 ± 2.38	7.99 ± 0.97	2.86
42	02:42:43.648	-00:00:50.941	23.48 ± 0.03	25.02 ± 0.02	64.14 ± 1.14	2.91 ± 0.85	2.61
43	02:42:38.955	-00:00:44.256	22.87 ± 0.03	24.33 ± 0.02	66.85 ± 2.34	34.72 ± 0.66	1.21
44	02:42:43.042	-00:00:37.908	23.82 ± 0.04	25.28 ± 0.03	68.69 ± 5.16	49.04 ± 1.67	1.61
45	02:42:40.974	-00:00:09.255	24.72 ± 0.04	25.98 ± 0.02	72.48 ± 3.24	70.62 ± 1.63	0.68
46	02:42:41.853	-00:01:32.254	24.05 ± 0.04	25.70 ± 0.04	73.83 ± 8.31	60.02 ± 2.03	1.95
47	02:42:39.674	-00:01:04.311	22.52 ± 0.03	23.94 ± 0.02	75.04 ± 4.07	68.65 ± 1.18	1.44
48	02:42:41.203	-00:01:32.948	24.51 ± 0.05	26.00 ± 0.04	79.11 ± 13.74	55.39 ± 2.90	1.47
49	02:42:38.652	-00:01:28.973	22.76 ± 0.03	24.67 ± 0.02	85.70 ± 4.06	82.38 ± 3.01	1.95
50	02:42:40.186	-00:01:26.054	24.19 ± 0.04	25.15 ± 0.02	90.31 ± 5.67	26.20 ± 1.34	1.01
51	02:42:42.400	-00:01:06.240	23.30 ± 0.03	24.94 ± 0.02	91.64 ± 3.98	49.90 ± 1.29	1.21

NOTE—The ID's of each Cepheid candidate correspond to the ID's of each light curve in Figure 9. The phases here are given in days with respect to the first visit. χ^2/ν is the reduced χ^2 value for the F555W Cepheid template fit.

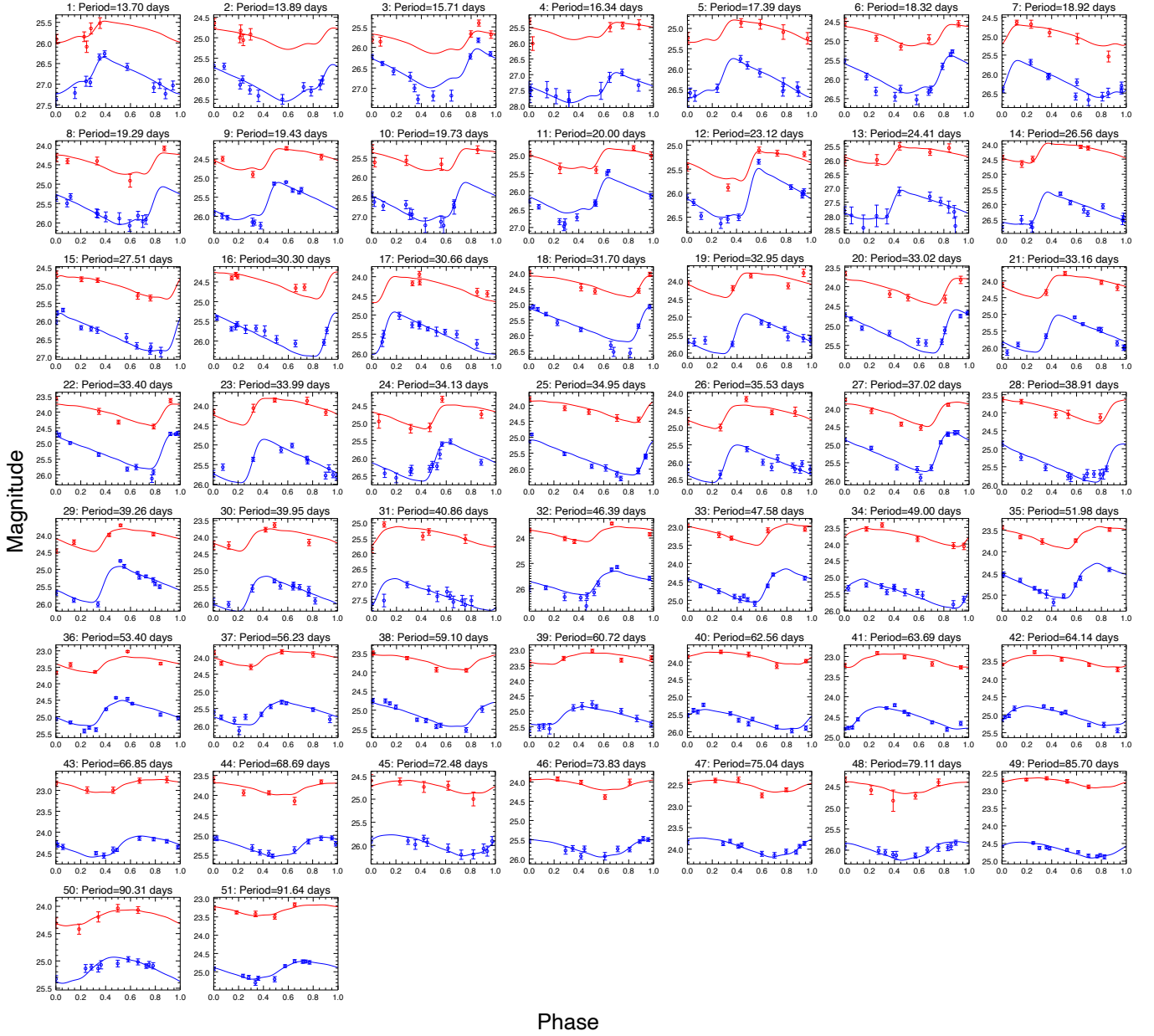


Figure 9. Light curves for 51 final Cepheid candidates in NGC 1068. The data points show the measurements in F555W (blue) and F814W (red), while the solid lines represent the best Cepheid template fits to the data.

REFERENCES

- Amiri, A., Knapen, J. H., Lehmer, B. D., & Khoram, A. 2025, *A&A*, 703, A161, doi: [10.1051/0004-6361/202556731](https://doi.org/10.1051/0004-6361/202556731)
- Anand, G. S., Lee, J. C., Van Dyk, S. D., et al. 2021, *MNRAS*, 501, 3621, doi: [10.1093/mnras/staa3668](https://doi.org/10.1093/mnras/staa3668)
- Antonucci, R. R. J., & Miller, J. S. 1985, *ApJ*, 297, 621, doi: [10.1086/163559](https://doi.org/10.1086/163559)
- Armah, M., Riffel, R., Dahmer-Hahn, L. G., et al. 2024, *MNRAS*, 534, 2723, doi: [10.1093/mnras/stae2263](https://doi.org/10.1093/mnras/stae2263)
- Asplund, M., Grevesse, N., & Sauval, A. J. 2005, in *Astronomical Society of the Pacific Conference Series*, Vol. 336, *Cosmic Abundances as Records of Stellar Evolution and Nucleosynthesis*, ed. T. G. Barnes, III & F. N. Bash, 25

- Asplund, M., Grevesse, N., Sauval, A. J., & Scott, P. 2009, *ARA&A*, 47, 481, doi: [10.1146/annurev.astro.46.060407.145222](https://doi.org/10.1146/annurev.astro.46.060407.145222)
- Bentz, M. C., Ferrarese, L., Onken, C. A., Peterson, B. M., & Valluri, M. 2019, *ApJ*, 885, 161, doi: [10.3847/1538-4357/ab48fb](https://doi.org/10.3847/1538-4357/ab48fb)
- Binggeli, B., Popescu, C. C., & Tammann, G. A. 1993, *A&AS*, 98, 275. <https://ui.adsabs.harvard.edu/abs/1993A&AS...98..275B>
- Binggeli, B., Sandage, A., & Tammann, G. A. 1985, *AJ*, 90, 1681, doi: [10.1086/113874](https://doi.org/10.1086/113874)
- Bono, G., Caputo, F., Fiorentino, G., Marconi, M., & Musella, I. 2008, *ApJ*, 684, 102, doi: [10.1086/589965](https://doi.org/10.1086/589965)
- Bose, S., & Kumar, B. 2014, *ApJ*, 782, 98, doi: [10.1088/0004-637X/782/2/98](https://doi.org/10.1088/0004-637X/782/2/98)
- Boselli, A., Voyer, E., Boissier, S., et al. 2014, *A&A*, 570, doi: [10.1051/0004-6361/201424419](https://doi.org/10.1051/0004-6361/201424419)
- Bottinelli, L., Gouguenheim, L., Fouque, P., & Paturel, G. 1990, *ApJ*, 82, 391
- Bottinelli, L., Gouguenheim, L., Paturel, G., & de Vaucouleurs, G. 1984, *A&A*, 56, 381
- Bottinelli, L., Gouguenheim, L., Paturel, G., & Teerikorpi, P. 1986, *A&A*, 156, 157
- Breuval, L., Kervella, P., Wielgórski, P., et al. 2021, *ApJ*, 913, 38, doi: [10.3847/1538-4357/abf0ae](https://doi.org/10.3847/1538-4357/abf0ae)
- Breuval, L., Riess, A. G., Macri, L. M., et al. 2023, *ApJ*, 951, 118, doi: [10.3847/1538-4357/acd3f4](https://doi.org/10.3847/1538-4357/acd3f4)
- Breuval, L., Riess, A. G., Casertano, S., et al. 2024, *ApJ*, 973, 30, doi: [10.3847/1538-4357/ad630e](https://doi.org/10.3847/1538-4357/ad630e)
- Brinks, E., Skillman, E. D., Terlevich, R. J., & Terlevich, E. 1997, *ApSS*, 248, 23, doi: [10.1023/A:1000519932279](https://doi.org/10.1023/A:1000519932279)
- Cantiello, M., Blakeslee, J. P., Ferrarese, L., et al. 2024, *ApJ*, 966, 145, doi: [10.3847/1538-4357/ad3453](https://doi.org/10.3847/1538-4357/ad3453)
- Cardelli, J. A., Clayton, G. C., & Mathis, J. S. 1989, *ApJ*, 345, 245, doi: [10.1086/167900](https://doi.org/10.1086/167900)
- Colina, L., Gonzalez Delgado, R., Mas-Hesse, J. M., & Leitherer, C. 2002, *ApJ*, 579, 545, doi: [10.1086/342839](https://doi.org/10.1086/342839)
- Csörnyei, G., Vogl, C., Taubenberger, S., et al. 2023, *A&A*, 672, A129, doi: [10.1051/0004-6361/202245379](https://doi.org/10.1051/0004-6361/202245379)
- Dametto, N. Z., Riffel, R., Colina, L., et al. 2019, *MNRAS*, 482, 4437, doi: [10.1093/mnras/sty2996](https://doi.org/10.1093/mnras/sty2996)
- Davies, R. I., Sugai, H., & Ward, M. J. 1998, *MNRAS*, 300, 388, doi: [10.1046/j.1365-8711.1998.01928.x](https://doi.org/10.1046/j.1365-8711.1998.01928.x)
- Davis, B. L., Graham, A. W., & Cameron, E. 2019, *ApJ*, 873, 85, doi: [10.3847/1538-4357/aaf3b8](https://doi.org/10.3847/1538-4357/aaf3b8)
- de Jaeger, T., Galbany, L., Riess, A. G., et al. 2022, *MNRAS*, 514, 4620, doi: [10.1093/mnras/stac1661](https://doi.org/10.1093/mnras/stac1661)
- de Vaucouleurs, G., de Vaucouleurs, A., Corwin, Jr., H. G., et al. 1991, *Third Reference Catalogue of Bright Galaxies*
- Dessart, L., & Hillier, D. J. 2005, *A&A*, 439, 671, doi: [10.1051/0004-6361:20053217](https://doi.org/10.1051/0004-6361:20053217)
- Edmunds, M. G., & Pagel, B. E. J. 1984, *MNRAS*, 211, 507, doi: [10.1093/mnras/211.3.507](https://doi.org/10.1093/mnras/211.3.507)
- Emsellem, E., Schinnerer, E., Santoro, F., et al. 2022, *A&A*, 659, A191, doi: [10.1051/0004-6361/202141727](https://doi.org/10.1051/0004-6361/202141727)
- Ferrarese, L., & Merritt, D. 2000, *ApJL*, 539, L9, doi: [10.1086/312838](https://doi.org/10.1086/312838)
- Ferrarese, L., Freedman, W. L., Hill, R. J., et al. 1996, *ApJ*, 464, 568, doi: [10.1086/177347](https://doi.org/10.1086/177347)
- Freedman, W. L., & Madore, B. F. 1990, *ApJ*, 365, 186, doi: [10.1086/169469](https://doi.org/10.1086/169469)
- . 2011, *ApJ*, 734, 46, doi: [10.1088/0004-637X/734/1/46](https://doi.org/10.1088/0004-637X/734/1/46)
- Freedman, W. L., Hughes, S. M., Madore, B. F., et al. 1994, *ApJ*, 427, 628, doi: [10.1086/174172](https://doi.org/10.1086/174172)
- Freedman, W. L., Madore, B. F., Gibson, B. K., et al. 2001, *ApJ*, 553, 47, doi: [10.1086/320638](https://doi.org/10.1086/320638)
- Fruchter, A. S., Hack, W., Dencheva, N., Droettboom, M., & Greenfield, P. 2010, in *2010 Space Telescope Science Institute Calibration Workshop*, 382–387
- García-Burillo, S., Combes, F., Usero, A., et al. 2014, *A&A*, 567, A125, doi: [10.1051/0004-6361/201423843](https://doi.org/10.1051/0004-6361/201423843)
- Gebhardt, K., Bender, R., Bower, G., et al. 2000, *ApJL*, 539, L13, doi: [10.1086/312840](https://doi.org/10.1086/312840)
- Graham, A. W., & Sahu, N. 2023, *MNRAS*, 518, 2177, doi: [10.1093/mnras/stac2019](https://doi.org/10.1093/mnras/stac2019)
- GRAVITY Collaboration, Pfuhl, O., Davies, R., et al. 2020, *A&A*, 634, A1, doi: [10.1051/0004-6361/201936255](https://doi.org/10.1051/0004-6361/201936255)
- Groves, B., Kreckel, K., Santoro, F., et al. 2023, *MNRAS*, 520, 4902, doi: [10.1093/mnras/stad114](https://doi.org/10.1093/mnras/stad114)
- Gámez Rosas, V., Isbell, J. W., Jaffe, W., et al. 2022, *Nat*, 602, 403, doi: [10.1038/s41586-021-04311-7](https://doi.org/10.1038/s41586-021-04311-7)
- Gámez Rosas, V., van der Werf, P., Gallimore, J. F., et al. 2025, *A&A*, 699, A187, doi: [10.1051/0004-6361/202453363](https://doi.org/10.1051/0004-6361/202453363)
- Gültekin, K., Richstone, D. O., Gebhardt, K., et al. 2009, *ApJ*, 698, 198, doi: [10.1088/0004-637X/698/1/198](https://doi.org/10.1088/0004-637X/698/1/198)
- Hamuy, M., Pinto, P. A., Maza, J., et al. 2001, *ApJ*, 558, 615, doi: [10.1086/322450](https://doi.org/10.1086/322450)
- Haynes, M. P., Giovanelli, R., Kent, B. R., et al. 2018, *ApJ*, 861, 49, doi: [10.3847/1538-4357/aac956](https://doi.org/10.3847/1538-4357/aac956)
- Hubble, E. P. 1925, *Obs*, 48, 139
- Jiménez-Bailón, E., Santos-Lleó, M., Mas-Hesse, J. M., et al. 2003, *ApJ*, 593, 127, doi: [10.1086/376554](https://doi.org/10.1086/376554)
- Kamenetzky, J., Glenn, J., Maloney, P. R., et al. 2011, *ApJ*, 731, 83, doi: [10.1088/0004-637X/731/2/83](https://doi.org/10.1088/0004-637X/731/2/83)
- Karachentsev, I. D., & Nasonova, O. G. 2013, *MNRAS*, 429, 2677, doi: [10.1093/mnras/sts557](https://doi.org/10.1093/mnras/sts557)
- Kennicutt, Jr., R. C. 1998, *ARA&A*, 36, 189, doi: [10.1146/annurev.astro.36.1.189](https://doi.org/10.1146/annurev.astro.36.1.189)

- Kennicutt, Jr., R. C., Stetson, P. B., Saha, A., et al. 1998, *ApJ*, 498, 181, doi: [10.1086/305538](https://doi.org/10.1086/305538)
- Kodric, M., Riffeser, A., Seitz, S., et al. 2015, *ApJ*, 799, 144, doi: [10.1088/0004-637X/799/2/144](https://doi.org/10.1088/0004-637X/799/2/144)
- Konigl, A., & Kartje, J. F. 1994, *ApJ*, 434, 446, doi: [10.1086/174746](https://doi.org/10.1086/174746)
- Kormendy, J., & Ho, L. C. 2013, *ARA&A*, 51, 511, doi: [10.1146/annurev-astro-082708-101811](https://doi.org/10.1146/annurev-astro-082708-101811)
- Kormendy, J., & Richstone, D. 1995, *ARA&A*, 33, 581, doi: [10.1146/annurev.aa.33.090195.003053](https://doi.org/10.1146/annurev.aa.33.090195.003053)
- Kourkchi, E., Courtois, H. M., Graziani, R., et al. 2020, *AJ*, 159, 67, doi: [10.3847/1538-3881/ab620e](https://doi.org/10.3847/1538-3881/ab620e)
- Kourkchi, E., & Tully, R. B. 2017, *ApJ*, 843, 16, doi: [10.3847/1538-4357/aa76db](https://doi.org/10.3847/1538-4357/aa76db)
- Leavitt, H. S., & Pickering, E. C. 1912, *HarCi*, 173, 1
- Lodato, G., & Bertin, G. 2003, *A&A*, 398, 517, doi: [10.1051/0004-6361:20021672](https://doi.org/10.1051/0004-6361:20021672)
- Macri, L. M., Stanek, K. Z., Bersier, D., Greenhill, L. J., & Reid, M. J. 2006, *ApJ*, 652, 1133, doi: [10.1086/508530](https://doi.org/10.1086/508530)
- Madore, B. F. 1982, *ApJ*, 253, 575, doi: [10.1086/159659](https://doi.org/10.1086/159659)
- Madore, B. F., & Freedman, W. L. 2024, *ApJ*, 961, 166, doi: [10.3847/1538-4357/acfaea](https://doi.org/10.3847/1538-4357/acfaea)
- . 2025, *ApJ*, 983, 161, doi: [10.3847/1538-4357/adbd3d](https://doi.org/10.3847/1538-4357/adbd3d)
- Martin, P., & Roy, J.-R. 1992, *ApJ*, 397, 463, doi: [10.1086/171803](https://doi.org/10.1086/171803)
- Mingozzi, M., Cresci, G., Venturi, G., et al. 2019, *A&A*, 622, A146, doi: [10.1051/0004-6361/201834372](https://doi.org/10.1051/0004-6361/201834372)
- Mochejska, B. J., Macri, L. M., Sasselov, D. D., & Stanek, K. Z. 2000, *ApJ*, 120, 810, doi: [10.1086/301493](https://doi.org/10.1086/301493)
- Nasonova, O. G., de Freitas Pacheco, J. A., & Karachentsev, I. D. 2011, *A&A*, 532, A104, doi: [10.1051/0004-6361/201016004](https://doi.org/10.1051/0004-6361/201016004)
- Pastorini, G., Marconi, A., Capetti, A., et al. 2007, *A&A*, 469, 405, doi: [10.1051/0004-6361:20066784](https://doi.org/10.1051/0004-6361:20066784)
- Pejcha, O., & Prieto, J. L. 2015, *ApJ*, 799, 215, doi: [10.1088/0004-637X/799/2/215](https://doi.org/10.1088/0004-637X/799/2/215)
- Pettini, M., & Pagel, B. E. J. 2004, *MNRAS*, 348, L59, doi: [10.1111/j.1365-2966.2004.07591.x](https://doi.org/10.1111/j.1365-2966.2004.07591.x)
- Pietrzyński, G., Graczyk, D., Gallenne, A., et al. 2019, *Nature*, 567, 200, doi: [10.1038/s41586-019-0999-4](https://doi.org/10.1038/s41586-019-0999-4)
- Pilyugin, L. S., & Grebel, E. K. 2016, *MNRAS*, 457, 3678, doi: [10.1093/mnras/stw238](https://doi.org/10.1093/mnras/stw238)
- Riess, A. G., Casertano, S., Yuan, W., Macri, L. M., & Scolnic, D. 2019, *ApJ*, 876, 85, doi: [10.3847/1538-4357/ab1422](https://doi.org/10.3847/1538-4357/ab1422)
- Riess, A. G., Yuan, W., Macri, L. M., et al. 2022, *ApJL*, 934, L7, doi: [10.3847/2041-8213/ac5c5b](https://doi.org/10.3847/2041-8213/ac5c5b)
- Riffel, R. A., Colina, L., Storchi-Bergmann, T., et al. 2016, *MNRAS*, 461, 4192, doi: [10.1093/mnras/stw1609](https://doi.org/10.1093/mnras/stw1609)
- Rodríguez, Ó., Clocchiatti, A., & Hamuy, M. 2014, *AJ*, 148, 107, doi: [10.1088/0004-6256/148/6/107](https://doi.org/10.1088/0004-6256/148/6/107)
- Romaniello, M., Primas, F., Mottini, M., et al. 2008, *A&A*, 488, 731, doi: [10.1051/0004-6361:20065661](https://doi.org/10.1051/0004-6361:20065661)
- Romaniello, M., Riess, A., Mancino, S., et al. 2022, *A&A*, 658, A29, doi: [10.1051/0004-6361/202142441](https://doi.org/10.1051/0004-6361/202142441)
- Roy, R., Kumar, B., Benetti, S., et al. 2011, *ApJ*, 736, 76, doi: [10.1088/0004-637X/736/2/76](https://doi.org/10.1088/0004-637X/736/2/76)
- Saha, A., Thim, F., Tammann, G. A., Reindl, B., & Sandage, A. 2006, *ApJS*, 165, 108, doi: [10.1086/503800](https://doi.org/10.1086/503800)
- Sakai, S., Ferrarese, L., Kennicutt, Jr., R. C., & Saha, A. 2004, *ApJ*, 608, 42, doi: [10.1086/386540](https://doi.org/10.1086/386540)
- Scheuermann, F., Kreckel, K., Anand, G. S., et al. 2022, *MNRAS*, 511, 6087, doi: [10.1093/mnras/stac110](https://doi.org/10.1093/mnras/stac110)
- Schinnerer, E., Maciejewski, W., Scoville, N., & Moustakas, L. A. 2002, *ApJ*, 575, 826, doi: [10.1086/341348](https://doi.org/10.1086/341348)
- Schinnerer, E., Leroy, A., Blanc, G., et al. 2019, *The Messenger*, 177, 36, doi: [10.18727/0722-6691/5151](https://doi.org/10.18727/0722-6691/5151)
- Schlafly, E. F., & Finkbeiner, D. P. 2011, *ApJ*, 737, 103, doi: [10.1088/0004-637X/737/2/103](https://doi.org/10.1088/0004-637X/737/2/103)
- Schöniger, F., & Sofue, Y. 1994, *A&A*, 283, 21
- . 1997, *A&A*, 323, 14
- Scoville, N. Z., Matthews, K., Carico, D. P., & Sanders, D. B. 1988, *ApJL*, 327, L61, doi: [10.1086/185140](https://doi.org/10.1086/185140)
- Seyfert, C. K. 1943, *ApJ*, 97, 28, doi: [10.1086/144488](https://doi.org/10.1086/144488)
- Shappee, B. J., & Stanek, K. Z. 2011, *ApJ*, 733, 124, doi: [10.1088/0004-637X/733/2/124](https://doi.org/10.1088/0004-637X/733/2/124)
- Shaya, E. J., Tully, R. B., Hoffman, Y., & Pomarède, D. 2017, *ApJ*, 850, 207, doi: [10.3847/1538-4357/aa9525](https://doi.org/10.3847/1538-4357/aa9525)
- Sofue, Y. 1991, *PASJ*, 43, 671
- Sparks, W. B. 1994, *ApJ*, 433, 19, doi: [10.1086/174621](https://doi.org/10.1086/174621)
- Spinoglio, L., Malkan, M. A., Smith, H. A., González-Alfonso, E., & Fischer, J. 2005, *ApJ*, 623, 123, doi: [10.1086/428495](https://doi.org/10.1086/428495)
- Stetson, P. B. 1987, *PASP*, 99, 191, doi: [10.1086/131977](https://doi.org/10.1086/131977)
- Telesco, C. M., Becklin, E. E., Wynn-Williams, C. G., & Harper, D. A. 1984, *ApJ*, 282, 427, doi: [10.1086/162220](https://doi.org/10.1086/162220)
- Thronson, Jr., H. A., Hereld, M., Majewski, S., et al. 1989, *ApJ*, 343, 158, doi: [10.1086/167693](https://doi.org/10.1086/167693)
- Tikhonov, N. A., & Galazutdinova, O. A. 2021, *AstBu*, 76, 255, doi: [10.1134/S199034132103010X](https://doi.org/10.1134/S199034132103010X)
- Tully, R. B., Courtois, H. M., & Sorce, J. G. 2016, *AJ*, 152, 50, doi: [10.3847/0004-6256/152/2/50](https://doi.org/10.3847/0004-6256/152/2/50)
- Tully, R. B., & Fisher, J. R. 1977, *A&A*, 54, 661
- . 1988, *Catalog of Nearby Galaxies*
- Tully, R. B., Rizzi, L., Shaya, E. J., et al. 2009, *AJ*, 138, 323, doi: [10.1088/0004-6256/138/2/323](https://doi.org/10.1088/0004-6256/138/2/323)
- Tully, R. B., Courtois, H. M., Dolphin, A. E., et al. 2013, *AJ*, 146, 86, doi: [10.1088/0004-6256/146/4/86](https://doi.org/10.1088/0004-6256/146/4/86)

- Udalski, A., Wyrzykowski, L., Pietrzynski, G., et al. 2001, *Acta Astron*, 51, 221, doi: [10.48550/arXiv.astro-ph/0109446](https://doi.org/10.48550/arXiv.astro-ph/0109446)
- Ulrich, M. H. 2000, *A&ARv*, 10, 135, doi: [10.1007/s001590000007](https://doi.org/10.1007/s001590000007)
- Venturi, G., Cresci, G., Marconi, A., et al. 2021, *A&A*, 648, A17, doi: [10.1051/0004-6361/202039869](https://doi.org/10.1051/0004-6361/202039869)
- Virtanen, P., Gommers, R., Oliphant, T. E., et al. 2020, *Nat Methods*, 17, 261, doi: [10.1038/s41592-019-0686-2](https://doi.org/10.1038/s41592-019-0686-2)
- Vogl, C., Kerzendorf, W. E., Sim, S. A., et al. 2020, *A&A*, 633, A88, doi: [10.1051/0004-6361/201936137](https://doi.org/10.1051/0004-6361/201936137)
- Welch, D. L., & Stetson, P. B. 1993, *AJ*, 105, 1813, doi: [10.1086/116556](https://doi.org/10.1086/116556)
- Yoachim, P., McCommas, L. P., Dalcanton, J. J., & Williams, B. F. 2009, *AJ*, 137, 4697, doi: [10.1088/0004-6256/137/6/4697](https://doi.org/10.1088/0004-6256/137/6/4697)
- Yoon, J. H., Putman, M. E., Thom, C., Chen, H.-W., & Bryan, G. L. 2012, *ApJ*, 754, 84, doi: [10.1088/0004-637X/754/2/84](https://doi.org/10.1088/0004-637X/754/2/84)
- Yuan, W., Fausnaugh, M. M., Hoffmann, S. L., et al. 2020, *ApJ*, 902, 26, doi: [10.3847/1538-4357/abb377](https://doi.org/10.3847/1538-4357/abb377)
- Yuan, W., Macri, L. M., Peterson, B. M., et al. 2021, *ApJ*, 913, 3, doi: [10.3847/1538-4357/abf24a](https://doi.org/10.3847/1538-4357/abf24a)
- Zasov, A. V., & Bizyaev, D. V. 1996, *AstL*, 22, 71